

Review Article

Applications of ultrafast wavefront rotation in highly nonlinear optics

F Quéré¹, H Vincenti^{1,2}, A Borot², S Monchocé¹, T J Hammond³,
Kyung Taec Kim³, J A Wheeler¹, Chunmei Zhang³, T Ruchon¹,
T Auguste¹, J F Hergott¹, D M Villeneuve³, P B Corkum³
and R Lopez-Martens²

¹ Commissariat à l'Énergie Atomique, Lasers, Interactions and Dynamics Laboratory (LIDyL), DSM/IRAMIS, CEN Saclay, F-91191 Gif sur Yvette, France

² Laboratoire d'Optique Appliquée, ENSTA-Paristech, Ecole Polytechnique, CNRS, F-91761 Palaiseau, France

³ Joint Attosecond Science Laboratory, National Research Council and University of Ottawa, 100 Sussex Drive, Ottawa ON, K1A 0R6, Canada

E-mail: fabien.quere@cea.fr

Received 6 March 2014, revised 22 April 2014

Accepted for publication 23 April 2014

Published 10 June 2014

Abstract

This paper provides an overview of ultrafast wavefront rotation of femtosecond laser pulses and its various applications in highly nonlinear optics, focusing on processes that lead to the generation of high-order harmonics and attosecond pulses. In this context, wavefront rotation can be exploited in different ways, to obtain new light sources for time-resolved studies, called 'attosecond lighthouses', to perform time-resolved measurements of nonlinear optical processes, using 'photonic streaking', or to track changes in the carrier-envelope relative phase of femtosecond laser pulses. The basic principles are explained qualitatively from different points of view, the experimental evidence obtained so far is summarized, and the perspectives opened by these effects are discussed.

Keywords: attosecond pulses, high-harmonic generation, ultrafast measurements, spatio-temporal couplings, femtosecond lasers, nonlinear optics

(Some figures may appear in colour only in the online journal)

1. Introduction

The extreme light intensities that can now be attained with femtosecond lasers have opened the field of highly nonlinear optics, where the response of a physical system exposed to the ultraintense laser field is non-perturbative [1, 2]. With the most powerful lasers now available, the optical response of electrons driven at relativistic velocities by the laser field can even be investigated [3].

One major outcome of this extreme regime of nonlinear optics in the last decade has been the generation, control, and measurement of attosecond pulses of light (1 as = 10^{-18} s), short enough to trigger and probe ultrafast electronic processes in matter [4–10]. The paradigm underlying the generation

of these pulses can be analysed both in the frequency and time domains. In the frequency domain, the highly nonlinear response of the system to the field results in the generation of many harmonic orders of the initial laser frequency, thus producing a spectrum that is broad enough to support attosecond pulses, provided the relative phase of these frequency components is adequate. In the time domain, these harmonics result from the periodic temporal distortion of the initially sinusoidal laser waveform, induced by the nonlinear interaction. If this distortion is well-localized in time on the scale of the laser optical period, attosecond pulses of light can be obtained by filtering out the fundamental frequency and keeping only the frequency components corresponding to this temporally well-localized distortion.

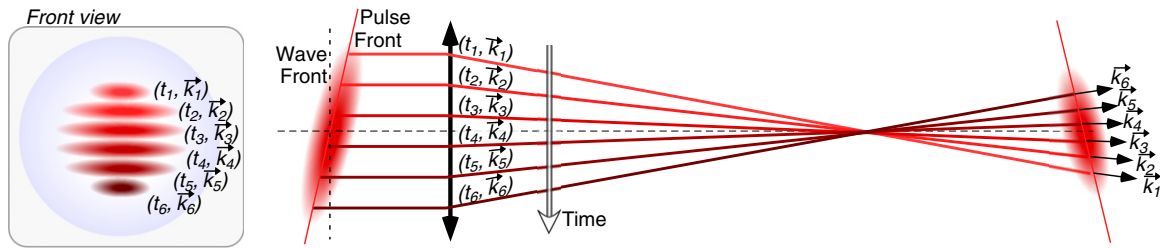


Figure 1. Focusing of a femtosecond beam exhibiting pulse front tilt. This figure illustrates how this PFT before focusing turns into a rotation in time of the light propagation direction at focus. The sketch labelled ‘front view’ shows that because of pulse front tilt, the effective position of the beam on the focusing optics shifts in time, leading to a temporal streaking of the focused light wave vector \mathbf{k} .

Measuring and controlling the processes that lead to the generation of these attosecond pulses has become a key issue for ultrafast science. For instance, motivated by the perspective of attosecond pump-probe experiments, many efforts have been devoted to the development of methods to generate single attosecond pulses, rather than the trains of pulses that are naturally produced during the successive laser periods of a multi-cycle laser pulse [6–11]. Such a control requires degrees of freedom on the laser field that can be manipulated on an ultrafast time scale. In the previous example, the polarization state of the laser field has been one of the key control parameters exploited so far [7, 8, 10]. However, its use is restricted to generation mechanisms that have a strong dependence on this polarization state.

More generally, controlling the interaction of ultraintense lasers with matter is now a key issue for all topics of high-field science, including processes that are very different from attosecond pulse generation, such as laser-driven particle acceleration. A central idea of this paper is that shaping light fields in both time and space can provide new degrees of freedom to manipulate matter with intense light, leading to new experimental capabilities. Laser fields whose spatial properties vary in time—or equivalently whose temporal properties vary in space—are said to be spatio-temporally coupled [12]. Here, we will discuss the use of a particular and very basic spatio-temporal coupling (STC) at the focus of a femtosecond laser, ultrafast wavefront rotation (WFR), which has first been explicitly discussed in [13].

We will first explain the basics of WFR, and how it can affect highly nonlinear optical processes such as the generation of attosecond light pulses by intense laser fields (section 2). We then show how this coupling can be exploited on the one hand to obtain a new type of light sources (section 3), called attosecond lighthouses, and on the other hand to perform ultrafast measurements with a resolution of the order of 1 fs, in a scheme called photonic streaking (section 4). Finally, the use of this effect to track changes in the carrier-envelope relative phase (CEP) of femtosecond lasers right in the interaction area with a target will be presented (section 5).

2. Wavefront rotation and its application to high-harmonic generation

WFR in time is a linear optical effect, that corresponds to a particular type of STC on a femtosecond laser beam. In this section, we first introduce key ideas about WFR and

its control in a simple and intuitive way, avoiding formal mathematical considerations. We then describe some of the physical effects that can occur when a femtosecond beam with such WFR is used to drive highly nonlinear optical effects in a medium. We will concentrate on the nonlinear effects that lead to the generation of attosecond pulses of light, such as those associated to high-order harmonic generation in gases [2] or plasmas [14]. In this case, WFR leads to some generic effects, irrespectively of the exact nonlinear mechanism responsible for the attosecond pulse generation.

2.1. Basics of wavefront rotation

The direction of propagation of light can vary during a femtosecond laser pulse: this is what physically corresponds to the STC called WFR. We only consider here the case where the rotation velocity of this propagation direction is constant in time, i.e. on what can be called linear WFR. It is intuitively very simple to understand how to generate such an effect. This basic principle is illustrated in figure 1, which shows the configuration of a femtosecond laser beam prior to focusing, and which leads to linear WFR once the beam is focused.

In figure 1, before focusing, the arrival time t_0 of the femtosecond laser pulse in a given plane z normal to the propagation direction (i.e. normal to the laser wavefront) varies linearly with the transverse coordinate x , $t_0(x) = \xi x + t_0(0)$. This results in a tilt of the location of the pulse maximum amplitude with respect to the wavefront, and this type of STC is therefore called pulse front tilt (PFT). ξ is the PFT parameter, which is typically expressed in fs mm^{-1} . PFT can be very easily induced, for instance by propagating the beam through a prism: because different parts of the beam travel through different thicknesses of glass, and because the group and phase velocities in glass are different, the wavefront and pulse front rotate by different amounts when crossing the prism, thus resulting in PFT. As we will see later, there are many other ways to induce PFT.

When the beam of figure 1 is sent on a focusing optics, its upper part intersects this optics before its lower part. In other words, in this configuration, the light field effectively sweeps across the aperture of the focusing optics as time evolves (see ‘front view’ in figure 1). As a result, the upper part of the beam in figure 1 reaches the focal point before its lower part. The delay between the arrival at focus of the two extreme sides of the beam is ξw_i , where w_i is the beam diameter on the focusing optics. This implies that the direction of light at focus sweeps

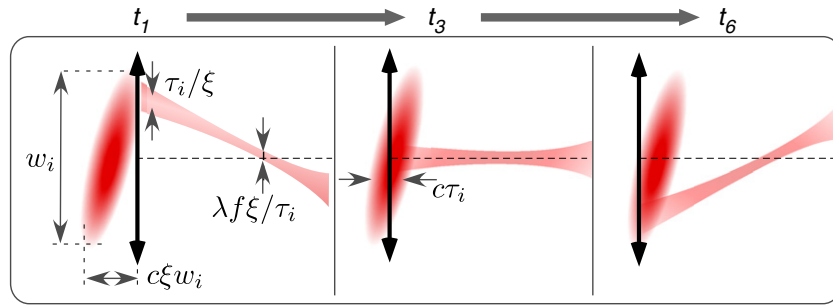


Figure 2. Detailed view of the focusing of a pulsed beam with PFT, at three different times t_1 , t_3 , t_6 (see figure 1 above). This sketch shows that for a large pulse front tilt ($\xi w_i \gg \tau_i$) the global duration of the beam (as defined in [15]) is ξw_i , and the effective beam width on the focusing optics at a given time is τ_i/ξ .

from the light red to the dark red arrow shown on figure 1 in this time interval. It is this change of the light propagation direction in time that leads to WFR at focus.

Focusing a femtosecond beam with PFT also has other consequences on the beam focus, which can be easily understood using the intuitive perspective provided by figure 1, and the more detailed view of figure 2. Indeed, since different parts of the beam reach the focus at different times, PFT leads to a temporal broadening of the pulse at focus. In the limit where $\xi w_i \gg \tau_i$ (where τ_i is the local laser pulse duration out of focus), the duration of the pulse at any point of the focus will obviously be ξw_i , which is the time required for the whole beam to sweep across the focusing optics. A rigorous calculation for Gaussian beams (both in the time and space domains) shows that the actual pulse duration at focus is $\tau_f = \tau_i \sqrt{1 + (\xi w_i/\tau_i)^2}$ [16]. Note that there is no more PFT on the beam at focus: the PFT applied on the beam prior to focusing has been converted into a totally different STC, as explained in [12, 13].

According to figure 2, because of PFT, only a fraction of the full beam aperture w_i contributes to the formation of the focal spot at a given time. For large ξ , the effective beam width on the focusing optics at a given time is of the order of $w_{\text{eff}} = \tau_i/\xi$. This implies that the size w_f of the focal spot along the direction of WFR is affected by this STC: assuming diffraction-limited focusing and large ξ , it is of the order of $w_f = \lambda f/w_{\text{eff}} = \lambda f \xi/\tau_i$, while it remains unchanged in the perpendicular direction, $w_0 = \lambda f/w_i$, leading to an elliptical focal spot. Like in the time domain, a more rigorous calculation for Gaussian beams shows that $w_f = w_0 \sqrt{1 + (\xi w_i/\tau_i)^2}$ [16].

The combination of these temporal and spatial broadenings results in the decrease of the peak intensity at focus, by a factor $1 + (\xi w_i/\tau_i)^2$. For this reason, residual PFT on high-power ultrashort laser beams is generally considered as detrimental for most experiments. This is in fact not an impediment for the use of WFR in high-field experiments, because as we will see below, the maximum value v_r^{max} of the WFR velocity $v_r = d\theta/dt$ occurs for a very moderate value of the PFT [16], and can thus be achieved without inducing a too severe distortion of the pulsed laser beam.

Figure 1 provides a very clear understanding of this optimum. Indeed, if the PFT ξ is very large, the laser beam then streaks the aperture of the focusing optics very slowly, leading to a small value of the WFR velocity. At the other extreme,

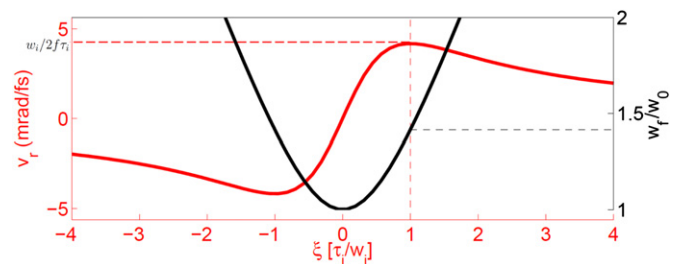


Figure 3. The red curve shows the evolution of the WFR velocity as a function of the PFT parameter ξ . The black curve shows the evolution with ξ of the ratio of the focal spot size along the direction of WFR, with the STC-free focal spot size. This also corresponds to the ratio of the actual pulse duration at focus with the STC-free Fourier-transform limited pulse duration τ_i .

if there is no PFT, v_r is obviously 0. The highest rotation velocity is thus achieved for an intermediate PFT, such that the beam streaks the focusing cone of the optics, of opening angle $\theta_L = w_i/f$, in the shortest possible time, which cannot be smaller than the Fourier-transform limited pulse duration τ_i . The maximum rotation velocity is thus expected to scale as $\theta_L/\tau_i = w_i/f\tau_i$. An exact calculation for Gaussian beams leads to $v_r^{\text{max}} = w_i/2f\tau_i$. Quite intuitively, considering figures 1 and 2, the shorter the laser pulse and/or the tighter the focusing, the higher the peak rotation velocity that can be achieved.

For Gaussian beams, the WFR velocity is given as a function of ξ by [16]:

$$v_r(\xi) = \frac{w_i^2}{f\tau_i^2} \frac{\xi}{1 + (w_i\xi/\tau_i)^2}. \quad (1)$$

The evolution of v_r with ξ is displayed in figure 3. The optimum described above is clearly observed. It occurs for a PFT of $\xi = \tau_i/w_i$, i.e. a time delay across the full diameter w_i of the unfocused beam equal to the initial pulse duration τ_i . At this optimum, compared to the STC-free case, the laser focal spot is elongated by a factor $\sqrt{2}$ along the direction of WFR, and the pulse duration is increased by the same factor, leading to a reduction of the peak intensity by a factor of 2 only.

We now present the connection between the point of view used here to explain WFR, and the one used in previous publications on this topic [16–18], which rather relied on the concept of spatial chirp. Both points of view are equally valid and useful, and strongly complementary. Figure 4 shows qualitatively that in a pulsed beam with PFT, the wavefronts

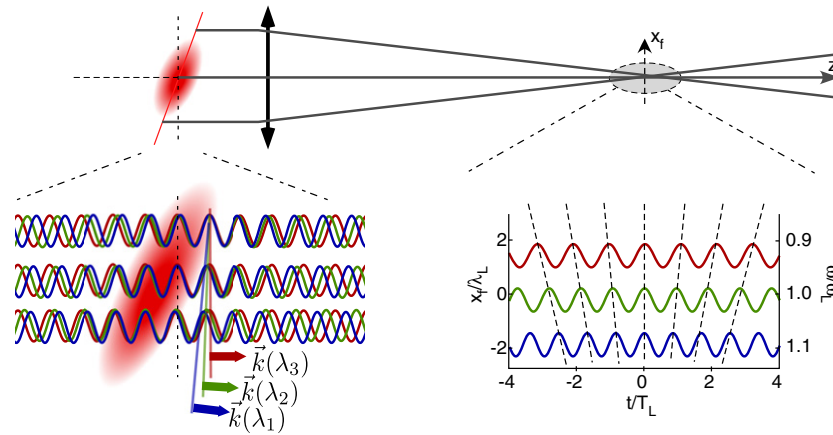


Figure 4. Complementary point of view on wavefront rotation at focus. The sketch on the left shows the different monochromatic waves making up a pulsed beam with PFT. The wavefronts on these different waves are not parallel, and they thus have different propagation directions. Formally, this comes from the fact that a delay τ in the time domain corresponds to a change in phase $\delta\varphi_\omega = \omega\tau$ for frequency ω . For a pulse front $t_0(x) = \xi x_i + t_0(0)$, and a wavefront perpendicular to the z -axis for frequency ω_0 , this leads to a phase front $\varphi_\omega(x) = \xi x_i(\omega - \omega_0)$ for frequency ω , which vary linearly with ω . These different frequency components are therefore focused at different locations, leading to spatial chirp at focus. The right sketch shows that this spatial chirp leads to wavefront rotation in time at focus.

of the different frequency components making up the pulse are not parallel—in other words, prior to focusing, the beam exhibits WFR in frequency, rather than in time. As a result, these frequency components propagate in different directions. This has been demonstrated more formally in [19], where Hebling showed that the PFT ξ and the spectral angular dispersion $d\Gamma/d\lambda$ (where $\Gamma(\lambda)$ is the angle of propagation of light at wavelength λ) of a beam are related by:

$$\tan c\xi = \frac{\bar{\lambda}}{\lambda} \frac{d\Gamma}{d\lambda} \quad (2)$$

with $\bar{\lambda}$ the mean wavelength of the beam. Incidentally, this shows that PFT can be induced not only by using a single prism, but more generally by propagating the beam through any optical system that results in spectral angular dispersion. This is for instance the case of a laser compressor where the relative angle between gratings or prisms is tuned. Note however that there are more complex ways of inducing PFT, in which this simple relationship is no longer valid. This kind of situation, not considered here, has been analysed in [12, 20, 21].

When such a beam is focused, the focal spots of the different frequency components will obviously be centred at slightly different transverse positions. As a result, the spectrum of the field changes with the transverse coordinate: this is called spatial chirp. This is the obvious result of the combination of an angularly-dispersive optical element with a focusing optics, which is nothing but a spectrometer. In the time domain, spatial chirp implies that the laser field oscillates at a central frequency that varies with the transverse coordinate. As explained in previous publications [16–18] and illustrated in figure 4, this naturally leads to WFR in time at focus.

Spatial chirp also provides a simple and alternative way of understanding the effects of PFT on the beam size and pulse duration at focus. The overall focal spot gets enlarged in one direction, because the different frequency components of the pulse are focused at different positions (while the size of the

focal spot of each frequency component remains unaffected). Spatial chirp also results in a narrowing of the local spectrum of the field at focus, which, for an initially Fourier-transform limited pulse, induces a temporal broadening.

We now conclude this subsection by noting that applying a linear PFT on the beam is not the only way to induce WFR at focus. A good illustration is the scheme recently proposed by Heyl *et al* [22, 23] to generate isolated attosecond pulses, called noncollinear optical gating, which is conceptually identical to the attosecond lighthouse effect but implements WFR in a different way.

In this scheme, two replicas of an initial laser beam are focused together in a medium. Before focusing, these two pulses are slightly shifted spatially (by a distance of the order of their diameter) and temporally. The total laser beam resulting from this combination exhibits what can be called a discrete or digitized PFT—i.e. the pulse front presents a sudden discontinuity in the middle of the beam. Just like continuous PFT discussed above, this naturally leads to spatial chirp and WFR at focus (in this case, only around the centre of the focal spot), provided the phase relationship between the two pulses is adequate. The WFR velocity gets optimal when the delay between the two pulses is of the order of the pulse duration, which is again similar to the case of continuous PFT.

2.2. Application to high-harmonic generation

The consequences of using a femtosecond laser beam with WFR at focus to generate high-order harmonics and attosecond pulses can be understood very intuitively, without referring to any detailed model of the generation process. We provide here two different and complementary qualitative analysis, in two different spaces.

The most intuitive understanding is achieved by considering the effects in the space with coordinates time and propagation angle [16–18]. When attosecond pulses are produced through the interaction of an intense laser field with

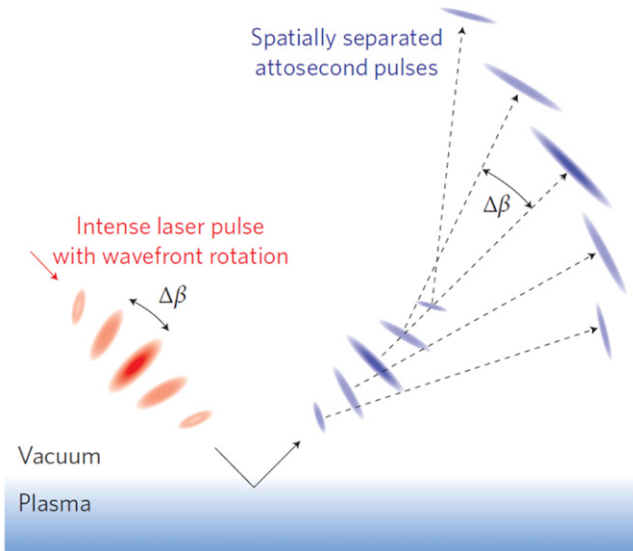


Figure 5. Illustration of the consequences of WFR on the attosecond pulses generated by an intense femtosecond laser pulse, in the case of plasma mirrors. Reprinted with permission from [17]. Copyright 2012 Nature Publishing Group.

a medium, they are emitted around certain phases of the field, typically once or twice every laser cycle (of duration T_L), depending on the symmetry of the system. As a first approximation, their propagation direction is along the normal of the instantaneous laser wavefront at the generation time. Thus, if the laser wavefront rotates in time with a velocity v_r , and if p attosecond pulses are emitted in each laser cycle ($p = 1$ or 2), a change $\Delta\beta = v_r T_L / p$ will be imprinted on the propagation directions of successive attosecond pulses.

When a multi-cycle laser pulse with WFR is used for the generation, it still produces a train of attosecond pulses at each point of the focus. But compared to the STC-free case, the propagation direction of each of these pulses is correlated to its emission time in the train. If properly optimized, this effect can be exploited to obtain, after diffraction from the source, separate beamlets for each individual attosecond pulses of the train generated at focus, as illustrated in figure 5. In order to achieve this complete angular separation of successive attosecond pulses, the angular shift $\Delta\beta$ obviously needs to be larger than the divergence θ_n of the attosecond pulses obtained by selecting a frequency window around the n th harmonic order, i.e.

$$\Delta\beta = v_r T_L / p \geq \theta_n. \quad (3)$$

As explained in the previous subsection, for given laser parameters, v_r has an upper value $v_r^{\max} = \theta_L / 2\tau_i$, where $\theta_L = w_i / f$ is the divergence of the focused laser beam used for the generation. Introducing this constraint in the previous equation leads to the following necessary condition to achieve a complete angular separation of the successive attosecond pulses:

$$\theta_n / \theta_L \leq \frac{1}{2pN_c} \quad (4)$$

with N_c the initial laser pulse duration (before focusing) expressed in laser periods T_L , i.e. $N_c = \tau_i / T_L$. What matters

is thus the number of periods in the driving laser pulse—not its absolute duration—as well as the ratio of the harmonic and laser divergences—not the absolute value of the harmonic divergence.

This shows that complete angular separation can only be achieved if the attosecond pulses have a significantly smaller divergence than the driving laser beam. This is the case in typical harmonic generation experiments, owing to the smaller wavelengths of the harmonics compared to the driving laser beam. The smaller the ratio of the harmonic and laser divergence, the longer the laser pulses that can be used to achieve the complete separation of the attosecond beamlets. The largest suitable pulse duration is given by $\tau_i^c = (\theta_L / 2p\theta_n) T_L$. Any pulse shorter than τ_i^c is also suitable: then it is no longer necessary to work at the optimum WFR velocity, so that weaker PFT can be used, with even less impact on the laser properties at focus.

An estimate of the *maximum* acceptable laser pulse durations required to achieve the complete angular separation can be made by considering the most favourable case, which occurs when the size of the harmonic beam in the generation medium is the same as (or comparable to) the laser focal spot size (i.e. the nonlinearity of the generation process is very weak), and the harmonic has a flat spatial phase in the source plane. In this case, $\theta_n / \theta_L = 1/n$, where n is the harmonic order. The condition given by equation (4) then leads to a maximum acceptable laser pulse duration τ_i^c :

$$\tau_i^c = (n/2p) T_L. \quad (5)$$

This equation shows that when few-cycle laser pulses are used ($\tau_i \approx 2$), complete angular separation can occur for all harmonic orders $n \gtrsim 4$ (assuming $p = 1$). For high-enough harmonic orders $n \geq 20$, equation (5) suggests that multi-cycle driving laser pulses can in principle be used to produce well-separated attosecond pulses ($\tau_i \geq 10T_L$ for $p = 1$, which corresponds to 25 fs for an 800 nm laser field). For so high-harmonic orders, however, the assumptions used to derive equation (5) are unlikely to be accurate (in particular, the harmonic source size is generally significantly smaller than the laser focal spot for such orders), so that this equation should then only be considered as a *necessary* condition. In this regime, the main issue is to keep a value of θ_n / θ_L close to its minimum $1/n$, as will be discussed in the next section.

We now briefly turn to an analysis of the effect in a different space, which coordinates are frequency and position at focus. According to the previous discussion, it is possible to generate a train of attosecond pulses at focus, and nonetheless obtain isolated attosecond pulses after propagation to the far-field. The latter have a continuous spectrum, while the former has a spectrum made of harmonic peaks, separated by spectral gaps. This at first sight seems to contradict a well-known principle of optics: the linear propagation of a light beam in a stationary medium does not affect its total frequency content, i.e. the spectral intensity of the light integrated in a plane normal to the propagation axis Oz does not vary with the z coordinate.

Figure 6 explains why there is in fact no contradiction. At each transverse position in the generation medium, a train

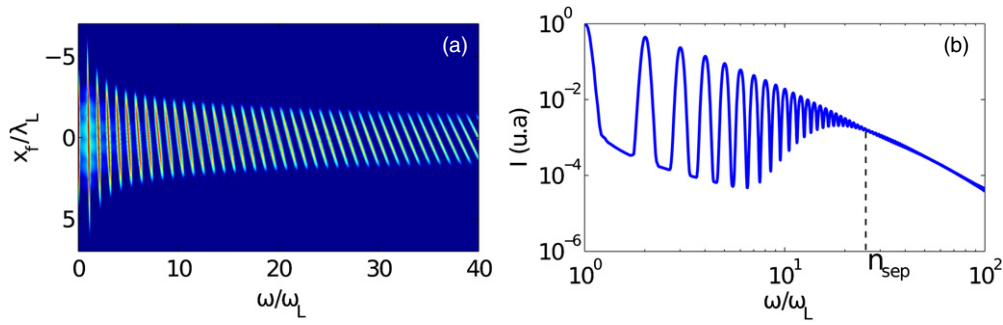


Figure 6. The left graph shows the spatially-resolved harmonic spectrum generated at the focus of a laser-field with spatial chirp (and hence WFR) as a function of the transverse coordinate x_f . The right graph shows the spatially-integrated spectral intensity of this beam, obtained by integrating the left graph along x_f . Due to the tilt of the harmonics, this spectrum becomes continuous beyond n_{sep} , potentially allowing for the generation of isolated attosecond pulses after propagation.

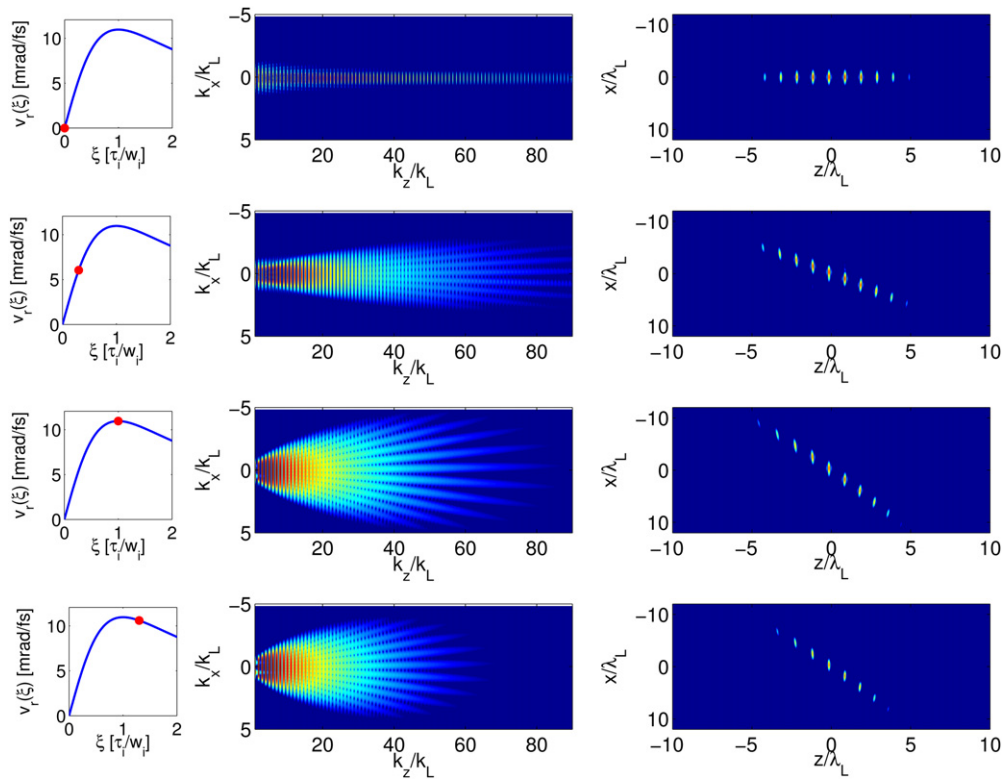


Figure 7. Simulation of the effect of an initial PFT applied to a laser driving HHG on a plasma mirror in the relativistic interaction regime (see section 4), for a laser pulse with $\tau_i = 10T_L$, $w_i = 70$ mm, focused with an optics of focal length $f = 200$ mm. The first column shows the WFR velocity achieved at focus, as a function of the PFT applied before focusing. The second one displays the 2D Fourier-transform of the harmonic field, in the (k_x, k_z) space, showing the harmonic spectrum that is generated and its angular properties. The third column shows a spatial intensity map of the attosecond pulses that are obtained after diffraction many Rayleigh lengths away from the source, by spectral filtering between the 70th and 80th harmonic orders.

of attosecond pulses is generated, associated in the spectral domain to a comb of harmonics. Due to the spatially-varying laser frequency $\omega_L(x_f)$ at focus, the frequencies of these harmonics vary in space, $\omega_n = n\omega_L(x_f)$. This is why the spatially-resolved harmonic peaks are tilted in figure 6(a). Due to this tilt, when the harmonic order reaches a large enough value n_{sep} , all spectral gaps get filled up in the spatially-integrated spectrum, which thus becomes continuous (figure 6(b)). This continuous integrated spectrum at focus is a required condition for the generation of isolated attosecond pulses in the far-field, since the subsequent propagation does not affect the total frequency content of the beam.

To conclude this part, figure 7 illustrates the evolution of the harmonic beams and attosecond pulses emitted upon the interaction of a laser pulse with a nonlinear medium, for different WFR velocities (as shown in the first column). The evolution from a train of attosecond pulses in the far-field, associated to a spectrum made of well-separated harmonic peaks, to a collection of angularly-separated isolated attosecond pulses, associated to continuous spectra, is clearly observed around the PFT that optimizes the WFR velocity. The details of the model used for this calculation are provided in [16, 24], but are not specified here since these effects

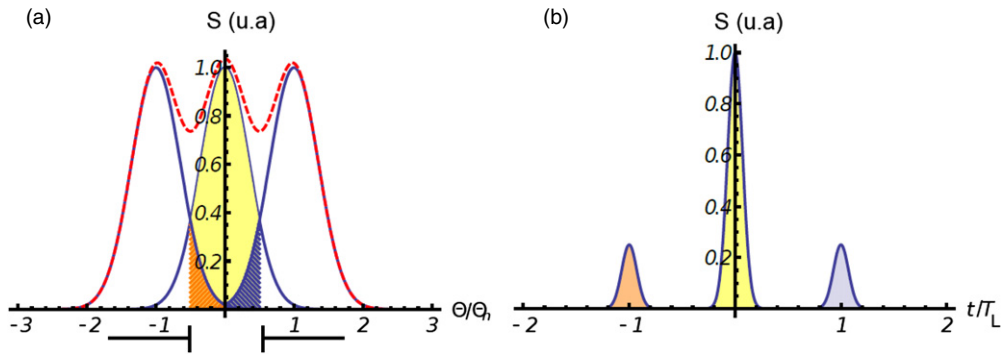


Figure 8. (a) Sketch of the angular profiles of three successive attosecond pulses emitted by an attosecond lighthouse. The blue Gaussians correspond to the angular profiles of these three individual attosecond pulses. The dashed red line, which is the sum of these three curves, corresponds to the signal that would be measured on a spatial detector in an experiment. The slit shown below the x -axis spatially filters the yellow part of the central beamlet, which corresponds to a fraction F of the central beamlet total energy. But this slit also lets the edges of the adjacent beamlets through (blue and orange hatched areas), which has consequences in the time domain. This is illustrated in (b), which shows the angularly-integrated temporal intensity profile of the field going through the slit. The central pulse, in yellow, corresponds to the yellow area in (a), while the satellite pulses in blue and orange are due to the blue and orange hatched areas in (a). The ratio in peak intensity between the satellite pulses and the central one is defined as γ , and is equal to 0.25 in this illustration. From the supplementary information of [16]. Reprinted with permission from [16]. Copyright 2011 American Physical Society.

correspond to a generic behaviour, independent of the exact generation mechanism that is involved.

In the next two sections, we discuss the different applications of this effect of WFR on high-order harmonic and attosecond pulse generation, for the generation of light sources and for ultrafast measurements.

3. Attosecond lighthouses as new light sources

The generation of isolated attosecond pulses is a crucial step towards time-resolved experiments with attosecond resolution, and has therefore been a key challenge in attosecond science since its very start [11]. WFR does not only provide a simple and elegant solution to this problem, but even enables the generation of a new type of light sources, called attosecond lighthouses, consisting in a collection of angularly-separated beamlets carrying isolated attosecond pulses. We first discuss the principle of these sources in more details, then present the first experimental evidence of attosecond lighthouses obtained in gases and plasmas, and compare this method to other approaches that have been used or proposed to generate isolated attosecond pulses. Attosecond lighthouses open new perspectives for attosecond science, which are discussed in the last subsection.

3.1. Key ideas

WFR makes it possible to obtain isolated attosecond pulses by inducing a ‘complete’ angular separation in the far-field of the adjacent attosecond pulses produced in the generation medium. We have already derived in subsection 2.2 the condition that needs to be fulfilled to achieve such an angular separation. This condition is however only qualitative: if the individual beamlets are assumed to have Gaussian spatial profiles, they always overlap to some extent and, strictly speaking, can never be fully-separated.

A quantitative analysis has been provided in the online supplementary information associated to [16]. We summarize here the key ideas and show some typical results. To obtain an

isolated attosecond pulse, a slit needs to be placed in the beam in the far-field, centred on one of the beamlets. In experiments, this spatial filtering can be achieved by the optics used to collect and manipulate this beamlet.

The optimum width l of this slit is the result of a compromise, as illustrated in figure 8. The larger the value of l , relative to the size of the beamlet, the larger the fraction F of the beamlet energy that is retained in this spatial filtering. But, on the other hand, a larger slit lets more of the adjacent beamlets through, and this degrades the temporal contrast ratio γ of the obtained attosecond pulse, which is a key parameter for attosecond pump-probe experiments.

The goal is thus to maximize F , i.e. to keep the largest possible fraction of the beamlet energy, while minimizing γ , i.e. getting the weakest possible satellite pulses in the time domain. The larger the angular separation $\Delta\beta$ (see figure 5 in previous section) between adjacent beamlets, relative to the divergence θ_n of the individual beamlets, the better this compromise can be. This angular separation increases with the WFR velocity, which can reach larger values when a driving laser pulse with fewer optical cycles is used.

This optimization problem can be expressed rather easily in mathematical terms, and the resulting equations are provided in the online supplementary information associated to [16]. We illustrate the results of this analysis in a particular case, where a driving laser pulse of initial duration $\tau_i = 9T_L$ (≈ 23 fs at 800 nm) is used at the optimum WFR velocity, and generates one attosecond pulse every period in a nonlinear medium.

Figure 9 plots, as a function of F and γ , the maximum acceptable ratio of the harmonic divergence and laser divergence, θ_n/θ_L , that is needed to be able to keep a fraction F of one of the generated beamlets, and at the same time achieve a temporal contrast ratio γ . This shows that for a broad range of retained energy fraction F , in order to obtain a contrast ratio between 1% and 10%, θ_n/θ_L needs to be slightly smaller than 0.1. Achieving such divergence ratios is in principle possible, but turns out to be rather challenging in practice. For this reason, as we will see in the next part, the initial experimental

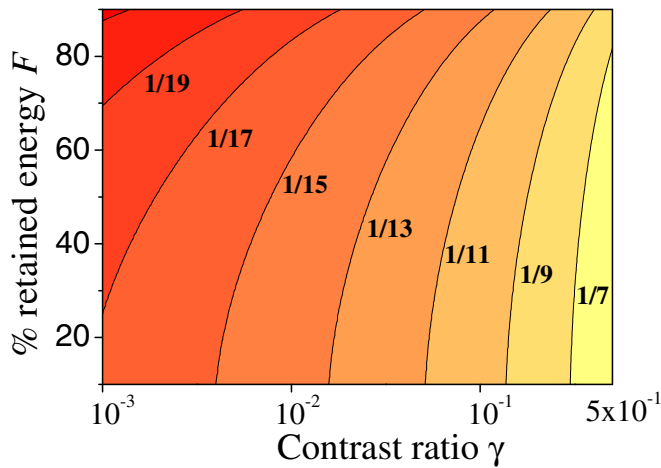


Figure 9. This graph plots the ratio of harmonic and laser divergences, θ_n/θ_L , that is required to obtain a single attosecond pulse produced by an attosecond lighthouse, with (1) a given intensity contrast ratio γ with its satellite pulses and (2) a fraction F of its total energy going through the slit used for spatial filtering. This calculation has been done for a driving laser pulse of $N_c = 9$ optical periods duration before focusing, and assuming $p = 1$ attosecond pulse generated per laser cycle. Larger values of θ_n/θ_L would be obtained for a shorter driving laser pulse.

demonstrations of attosecond lighthouses have been achieved with significantly shorter pulses ($N_c \approx 2-3$), which allow for larger WFR velocity, and hence make it possible to achieve a good angular separation of adjacent attosecond pulses even with larger values of θ_n/θ_L .

3.2. Experimental and numerical evidence in gases and plasmas

We now turn to the first experimental demonstrations of the generation of attosecond lighthouses. Two experiments have been performed shortly after the theoretical analysis of this

effect: the first one on harmonics generated from initially solid targets, performed at Laboratoire d’Optique Appliquée (salle noire laser) in France [17], and the second one on harmonics generated in gases, at the National Research Council of Canada [18]. In order to achieve high WFR velocities, both experiments used few-cycle long driving laser pulses, provided by 1 kHz phase-stabilized laser systems, post-compressed after spectral broadening in a hollow-core fibre. In both cases, an adjustable amount of PFT was introduced on the laser beam prior to focusing, simply by rotating one of the prisms in the pair used to fine tune the duration of the few-cycle laser pulse, as sketched on figures 10 and 12. This led to an adjustable WFR velocity at focus, where harmonic generation occurs on the target.

In the first experiment [17], the laser beam was focused onto a rotating fused silica target using an off-axis parabolic mirror, with a numerical aperture of $f/1.7$ leading to a focal spot size of $1.8 \mu\text{m}$. With a pulse duration of 7 fs, the $\approx 1 \text{ mJ}$ pulse energy resulted in a peak intensity at focus estimated to be just below $10^{18} \text{ W cm}^{-2}$. At these intensities, the surface of the solid target gets fully ionized early in the rising edge of the laser pulse, resulting in the formation of a dense plasma, which is reflective for the incident laser. For femtosecond durations, the plasma expansion during the laser pulse remains very weak. The plasma-vacuum interface thus remains optically-flat, forming what is called a plasma mirror, which specularly reflects the laser beam. At ultrahigh laser intensities, the response of the plasma mirror to the field becomes nonlinear, and high-order harmonics, associated in the time domain to a train of attosecond pulses [25], are generated upon reflection of the beam. In the conditions of the experiment described here, this occurred through a mechanism known as coherent wake emission (CWE) [26].

Two different diagnostics were used to study this emission. The first one measures the angularly-resolved spectrum in the extreme ultraviolet (XUV) (last column

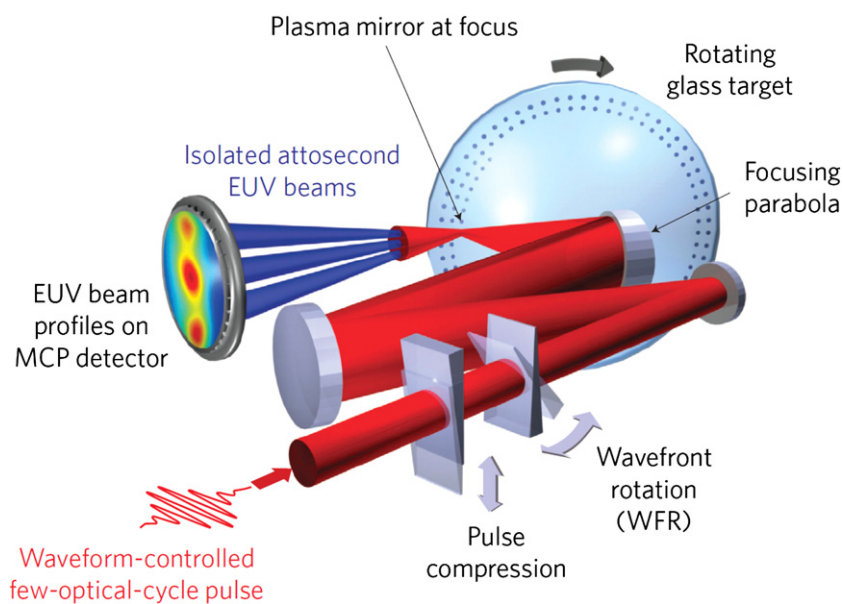


Figure 10. Schematic of the experiment performed at LOA on harmonics generated through the CWE mechanism on plasma mirrors created on initially solid targets, at intensities $\approx 10^{18} \text{ W cm}^{-2}$. Reprinted with permission from [17]. Copyright 2012 Nature Publishing Group.

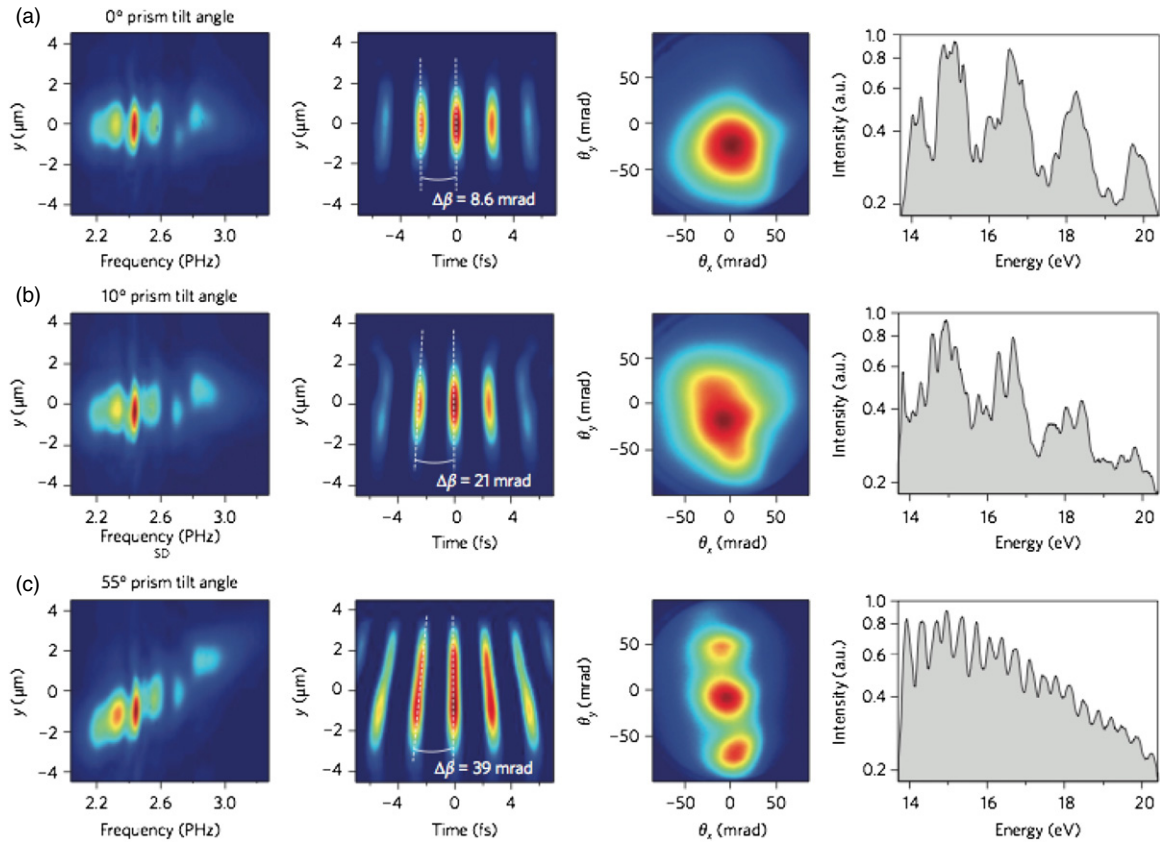


Figure 11. Main experimental results of the LOA experiment. Left column: spatially resolved spectra of the driving laser field at focus for an increasing relative tilt of the prisms (0, 10 and 55° for (a)–(c), respectively). Second column: calculated laser electric field $E(y, t)$ at focus (with the blue-to-red colour scale corresponding to values of $E \geq 0$, while all values of $E \leq 0$ are displayed in dark blue), deduced from the first column by a Fourier-transform with respect to frequency, assuming a constant phase in space and frequency. Third column: measured spatial EUV beam profile for a fixed arbitrary value of the CEP of the laser. Rightmost column: corresponding EUV spectra recorded at the centre of the spatial beam profile. Reprinted with permission from [17]. Copyright 2012 Nature Publishing Group.

in figure 11). Given the large divergence of the laser and harmonic beam, it only captures a small fraction of the XUV beam near its centre. The other diagnostic, sketched in figure 10, simply records the spatial profile of the reflected beam in the XUV (third column in figure 11). The laser beam itself is diagnosed at focus by measuring the spatially-resolved spectrum along the direction of WFR (first column in figure 11), to determine the spatial chirp at focus that results from the rotation of the prism. Assuming Fourier-transform limited pulses, this makes it possible to determine the WFR velocity, simply by performing a Fourier-transform with respect to frequency to obtain the laser field in time and space (second column in figure 11).

Figure 11 shows the evolution of these different quantities when the PFT applied on the beam prior to focusing is increased. When no PFT is introduced (first line), the laser spectrum at focus hardly varies across the focal spot, leading to a wavefront velocity close to zero. All the attosecond pulses are then emitted along the same direction, and we detect a single XUV beam on the detector, with a spectrum consisting of harmonic-like peaks [27]. When PFT is intendedly introduced by rotating one of the prisms (second line), the laser beam has spatial chirp at focus, leading to a WFR in time. The harmonic beam then starts to elongate in the direction where PFT has been induced. Finally, in the last line of figure 11, the amount

of spatial chirp has been increased until the rotation angle $\Delta\beta$ of the wavefront in one laser period reaches the considerable value of 39 mrad. Note that due to the tight focusing geometry and the short duration of the laser pulse, the maximum possible value of $\Delta\beta$ achievable in this experiment was estimated to be even larger, around 80 mrad. In these conditions, the observed XUV beam consists of a collection of well-separated beamlets. According to the discussion of subsection 2.2, each of these beamlets corresponds to a single attosecond pulses, a conclusion that is supported by the fact that the spectrum of the central beamlet is now continuous.

Even after the principle of attosecond lighthouses had been clearly established in the case of HHG from plasma mirrors, first by numerical simulations [16] and then by the experiment just described [17], the applicability of this scheme to HHG in gases initially remained unclear: this generation scheme involves both propagation and phase matching effects in the generation medium, which were considered to potentially complicate the effect of WFR on the generated attosecond pulses. This issue was first solved in [18], which presented experimental and numerical results unambiguously demonstrating that in appropriate conditions, attosecond lighthouses can also be generated from gases. Note that this is in principle slightly more demanding than HHG from plasma mirrors, since in the former case two attosecond

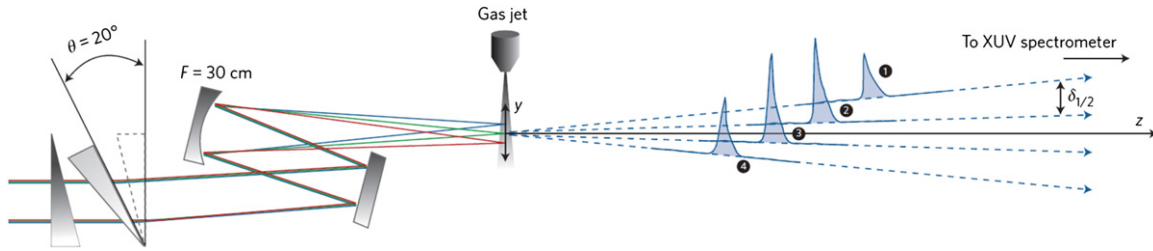


Figure 12. Schematic of the experiment performed at NRC on harmonics generated in atomic and molecular gases, at intensities $\approx 10^{14}$ W cm $^{-2}$. Reprinted with permission from [18]. Copyright 2013 Nature Publishing Group.

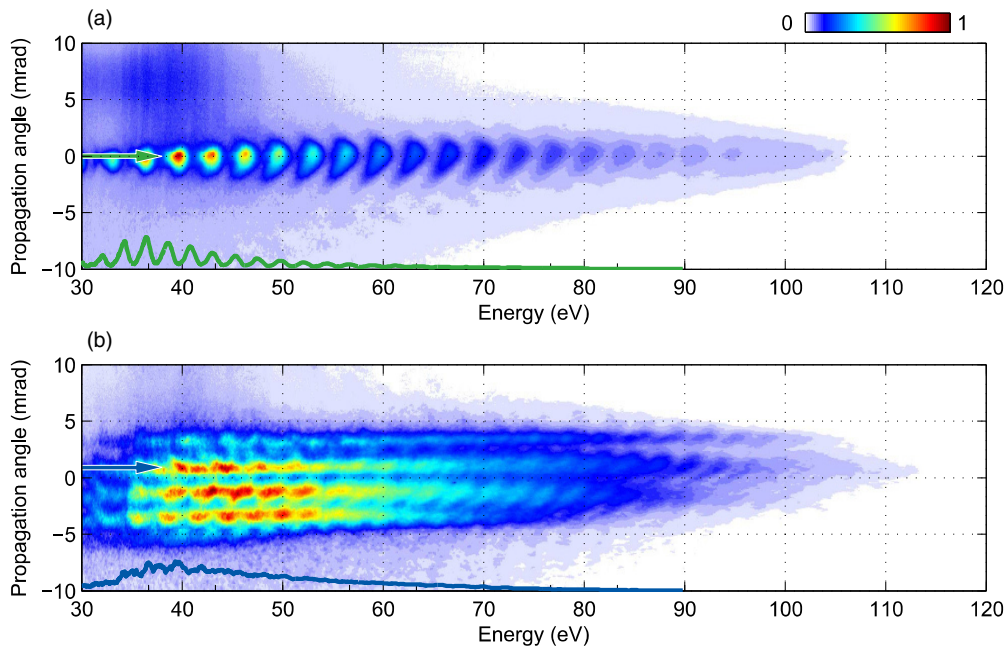


Figure 13. Main experimental results of the NRC experiment. Panels (a) and (b) show the angularly resolved XUV spectrum (colour map) generated in Ne without (a) and with (b) WFR, in linear colour code. At the bottom of each graph, the XUV spectrum at one angle (indicated by the horizontal arrow) is shown by the solid lines. Note that the CEP of the laser was stabilized in (b), but not in (a). Reprinted with permission from [18]. Copyright 2013 Nature Publishing Group.

pulses are generated in each laser cycle ($p = 2$), instead of one only ($p = 1$) in the later case. In gases, twice shorter laser pulses are thus required to achieve the same angular separation $\Delta\beta$ between successive attosecond pulses as in the case of plasma mirrors, assuming identical focusing conditions.

The set-up of the experiment performed in gases is sketched in figure 12. The laser beam was focused onto a gas jet (Ne or N $_2$) with an off-axis parabolic mirror of 300 mm focal length, leading to peak intensity of up to a few 10^{14} W cm $^{-2}$. The diagnostic, as in the previous experiment, consisted in measuring the angularly-resolved XUV spectrum. However, in this case, because the divergence of the beam was much smaller than in the previous experiment due to the looser focusing of the driving laser beam, it was possible to simultaneously measure the spectra of all the beamlets produced by the lighthouse effect. This led to the type of results displayed in figure 13. Panel (a) shows the measurements in the absence of PFT on the driving beam. A single XUV beam is observed, with a spectrum consisting of well-separated harmonic peaks (except near the spectral cut-off), typical of a train of attosecond pulses. When a PFT leading to a

significant WFR velocity at focus is introduced, this beam splits in a collection of ≈ 4 beamlets, as is expected in the attosecond lighthouse effect. The spectrum of each beamlet is only slightly modulated in amplitude, due to the slight residual overlap between adjacent beamlets, that leads to weak satellite attosecond pulses in the time domain. These beamlets correspond to the individual attosecond pulses emitted every half laser optical period in the generation medium.

A question that is often raised about this attosecond lighthouse effect is how it affects the individual attosecond pulses, and more specifically whether or not WFR induces significant STC on these pulses, that would spoil their duration and prevent their use in time-resolved experiments. The intuitive answer is that, because WFR is significant on the scale on the laser optical period (2.6 fs for an 800 nm wavelength) but very weak on the attosecond time scale, hardly any distortion is expected on individual attosecond pulses. In fact, the STC potentially induced on the attosecond pulses are best understood by considering the laser field configuration at focus, which is characterized by a spatial chirp. Because the harmonic spectral intensity and spectral phase generally depend on the driving laser central wavelength,

this spatial chirp implies that the exact temporal properties of the attosecond pulses produced at focus in principle change with the radial coordinate. This potentially leads to high-order STC, such as a spatially-dependent attosecond temporal chirp. But this variation of the harmonic emission properties is moderate over the spectral width of the driving laser pulse, so that these STC are expected to be weak.

These qualitative answers could not be validated in the two previous experiments, since no temporal measurement was performed on the individual beamlets, and spatio-temporal metrology of attosecond pulses is anyway still in a very early stage [28]. But this issue can be addressed accurately in numerical simulations, which are now very reliable both for gases and plasmas. To this end, we use 2D particle-in-cell simulations with the CALDER code in the case of plasmas. For HHG in gases, we used a standard 2D simulation code, described in [29, 30] and summarized in section 2 of the supplementary material of [18], and which in particular takes into account phase matching and propagation effects (both for the laser and the harmonic beams).

The results of such simulations are displayed in figures 14–16, where the attosecond pulses obtained without and with WFR are compared, for the two generation processes occurring on plasma mirrors (CWE in figure 14 and the relativistic oscillating mirror (ROM) in figure 15—see section 3.4 about this mechanism), and for HHG in gases (figure 16). In all cases, the individual attosecond pulses generated with WFR have a temporal structure similar to the ones obtained without WFR. No significant low-order STC such as PFT is observed either on these pulses, nor any higher order STC, such as pulse front curvature or a variation of the temporal structure across the beam. As a result, the *spatially-integrated* temporal intensity profile of a single attosecond pulse, isolated by the lighthouse effect, is almost identical to the one of the same pulse within the attosecond pulse train produced in the absence of WFR. This demonstrates that the attosecond lighthouse effect hardly alters the duration of individual attosecond pulses.

3.3. Comparison with other temporal gating techniques

Several other methods have been developed for both gas and plasmas in the pursuit of generating isolated attosecond pulses [11, 31, 32]. In gases, the main gating techniques are:

- (i) *High frequency filtering*. This consists in using a few-cycle laser pulse for the generation, and filtering the high-frequency end of the obtained XUV spectrum [9]. In gases, the harmonic spectral cut-off depends on the laser intensity, so that the highest harmonics are only generated around the peak of the laser pulse, which can amount to a single half-laser-cycle—hence leading to a single attosecond pulse—if the laser pulse is short enough, and for an appropriate CEP of the field [33, 34].
- (ii) *Polarization gating*. This consists in using a laser pulse which polarization state progressively varies from circular to linear and then back to circular. Since HHG in gases is suppressed for ellipticities $\epsilon \gtrsim 0.1$, a single attosecond pulse can be obtained if the variation of ϵ in time is fast enough [7, 35, 36].

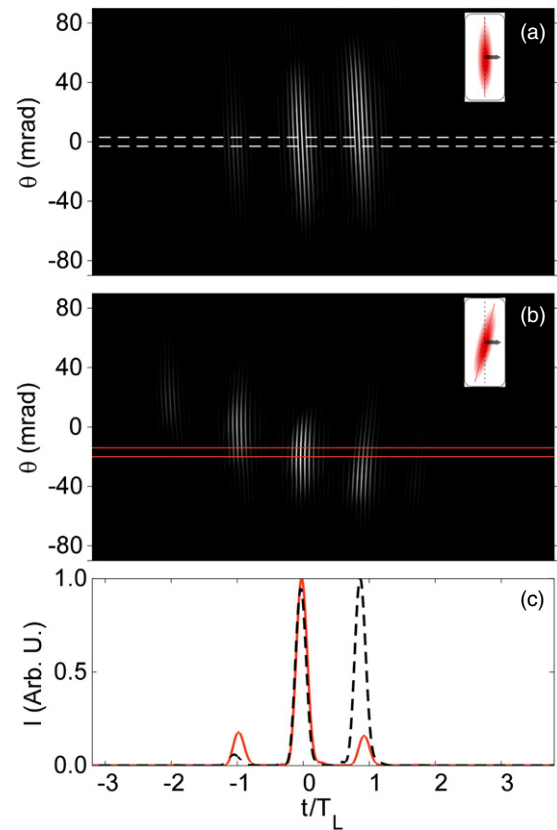


Figure 14. Results of 2D particle-in-cell simulations for HHG from plasma mirrors performed with the CALDER code in the CWE regime (5 fs initial pulse duration τ_i with a peak intensity $7 \times 10^{17} \text{ W cm}^{-2}$, density gradient scale length $\lambda_L/70$, 45° incidence, p -polarization). Panel (a) corresponds to the case without WFR, while in panel (b), WFR has been introduced with an optimized velocity. Both panels display the E -field obtained by filtering the reflected radiation between harmonics 8 and 13, after the pulses have propagated away from the target a distance large compared to the Rayleigh length of the EUV radiation. This field is plotted as a function of time and propagation angle. Panel (c) plots the corresponding temporal intensity profiles (dashed black, without WFR-red, with WFR), spatially integrated between the horizontal lines shown in panels (a) and (b), of equal widths.

- (iii) *Ionization gating*. This consists in adjusting the generation conditions in such a way that the ionization of the generation medium—which leads to depletion of the generating atoms and/or affects phase matching—acts as a temporal gate. When properly optimized, this leads to the generation of isolated attosecond pulses [37–43].

All these schemes have been demonstrated experimentally and validated numerically. Note that they all require a stabilization of the laser CEP in order to ensure shot-to-shot reproducibility of the generated attosecond pulses. They can be combined with $\omega - 2\omega$ mixing, where a small amount of second harmonic 2ω is added to the fundamental driving laser frequency ω [44]. Adjusting the relative power and phase of these two frequencies can result in the emission of only one attosecond pulse per optical period of the fundamental frequency. This leads to a larger time interval between successive attosecond pulses, and thus facilitates the isolation of a single pulse. The combination of $\omega - 2\omega$ mixing and

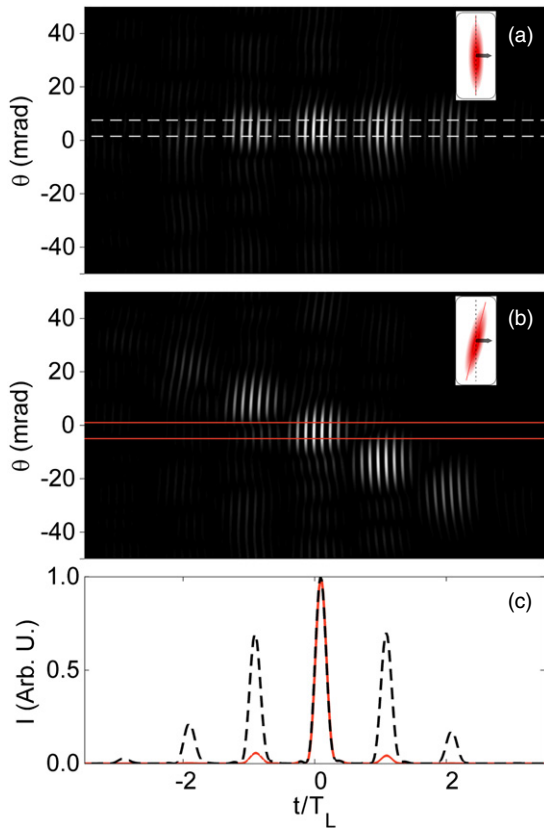


Figure 15. Results of 2D particle-in-cell simulations for HHG from plasma mirrors performed with the CALDER code in the ROM regime (17 fs initial pulse duration τ_i with a peak intensity $7.8 \times 10^{19} \text{ W cm}^{-2}$, density gradient scale length $\lambda_L/200$, 45° incidence, p -polarization). The quantities that are plotted are the same as in figure 14, except that here the harmonics have been filtered between orders 18 and 23.

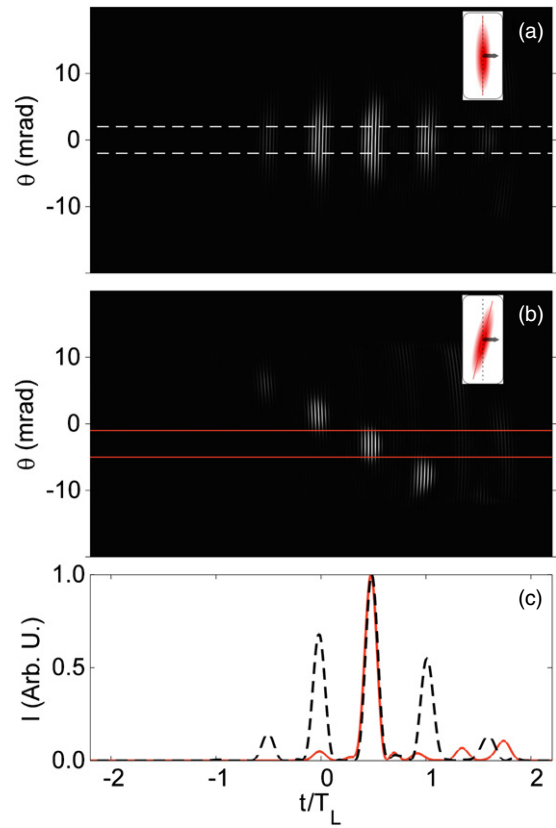


Figure 16. Results of 2D simulations for HHG from gases (5 fs initial pulse duration τ_i with a peak intensity $5 \times 10^{14} \text{ W cm}^{-2}$, focused with a Rayleigh length of $400 \mu\text{m}$, $200 \mu\text{m}$ before a Ne gas medium with a super Gaussian density profile of $100 \mu\text{m}$ length and 10 mbar pressure). The quantities that are plotted are the same as in figures 14 and 15, except that here the harmonics have been filtered between orders 20 and 120 (which includes all the plateau harmonics).

polarization gating—a scheme known as double optical gating (DOG)—has proved very successful [10, 45].

In the case of plasma mirrors, different gating techniques have been proposed theoretically, which have been largely inspired by the schemes developed for gases. However, these schemes suffer from severe limitations, which have prevented their experimental demonstration so far.

- (i) *High frequency filtering.* This is the same idea as in gases [46], but a practical impediment is that it is challenging, although possible, to generate few-cycle pulses with enough energy to reach the intensities required for HHG from plasmas. In addition, this idea does not apply to CWE, for which the harmonic spectrum hardly depends on laser intensity. As a result, driving CWE with few-cycle pulses still leads to the emission of attosecond pulse trains [27].
- (ii) *Polarization gating.* Like in gases, HHG from plasmas can be sensitive to the ellipticity of the field [47]. However, this is restricted to near-normal incidence on target, because for oblique incidence HHG occurs even with circularly polarized light. This is a serious drawback of this scheme, since the generation efficiency gets strongly reduced at near-normal incidence. In addition, generating a time-

varying ellipticity is challenging with the high-power lasers used for HHG from plasmas.

- (iii) *The λ^3 scheme.* The main idea consists in focusing very tightly (area $\approx \lambda^2$) a short laser pulse on a slightly overdense plasma in order to deform its critical surface in time, and thus to dynamically change the reflection angle of the laser, i.e. the direction of emission of the attosecond pulses [48]. This interesting idea suffers from several drawback. Numerical simulations show that this only provides isolated attosecond pulses when few-cycle laser pulses are used (hence the name λ^3), like in high frequency filtering. Moreover, it is difficult to create a plasma with a density equal to a few times the critical density. Finally, this technique hardly provides any control on the direction of emission of the attosecond pulses, which makes it difficult to use in any application experiment.

The last two schemes have not been demonstrated experimentally yet. For high frequency filtering, only some indirect evidence has been obtained [49], in the ROM regime (see next subsection 3.4 about this mechanism), but without shot-to-shot reproducibility due to the lack of CEP stabilization. To date, the only clear evidence of isolated

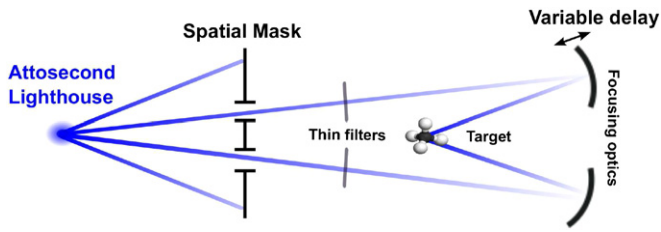


Figure 17. Possible schematic for an attosecond pump-attosecond probe experiment using an attosecond lighthouse source.

attosecond pulses generated from plasmas was obtained using the attosecond lighthouse scheme [17].

Compared to all these gating technique, the lighthouse effect has several very significant advantages. It is universal, i.e. it in principle applies to any HHG mechanism that leads to the generation of attosecond pulses, provided the condition given by equation (4) can be fulfilled. It is the only scheme that generates a collection of spatially-separated isolated attosecond pulses in well-controlled directions, which has promising applications for time-resolved experiments, as described in the next subsection. The implementation of this gating scheme is of unprecedented simplicity, since it only requires a slight rotation of one of the optics in the typical laser chains used for HHG. As opposed to high frequency filtering, it isolates the attosecond pulses over the almost entire spectral bandwidth of the emission, as polarization gating does. But, as opposed to polarization gating, it only weakly affects the generating conditions and hardly compromises the generation efficiency, and can be implemented at different laser wavelengths (e.g. in the far infrared) in a very straightforward way. Finally, it has the potential to generate isolated attosecond pulses with many-cycle long driving laser pulses, possibly at the cost of a slightly more complicated experimental scheme, as discussed in the next subsection.

3.4. Future applications and evolutions of the scheme

In terms of applications, the fact that attosecond lighthouses provide a collection of spatially-separated and perfectly-synchronized isolated attosecond pulses opens very interesting perspectives. This scheme is well-suited to future attosecond pump-probe experiments, since a selection of some of the beamlets could be refocused on a target with variable delays. In the simplest of these schemes, one of the beamlets would be used as a pump, and another as a probe, as illustrated in figure 17. More sophisticated schemes can be foreseen, which will be discussed in the conclusion.

A potential problem in this kind of scheme is the loss of temporal resolution occurring because of the crossing angle between the different beams in the medium. This could be an impediment for experiments that really require the ultimate temporal resolution determined by the duration of the attosecond pulses. This temporal blurring can however be minimized by an optimized focusing geometry of the different beamlets, for instance by focusing one beam much more tightly than the other in the target medium. It can even be overcome in different ways. One is to perform spatially-resolved measurements on the probe beam, in which case the

temporal blurring can be taken into account and eliminated in the data analysis. For measurements performed on particles emitted by the system, where the previous solution cannot be applied, a solution to eliminate this blurring—which is however technologically challenging—would be to induce adequate PFT's at focus on the different attosecond beamlets, as is done for the optimization of noncollinear sum-frequency generation.

In the perspective of such applications, a key technical challenge to address in the coming years will be to obtain attosecond lighthouses with longer driving laser pulses. As discussed before, this is in principle possible, but it requires getting small values of the ratio θ_n/θ_L of the harmonic and laser beam divergences, as close as possible to the minimum value $1/n$. In practice, the main difficulty to achieve this condition is to mitigate the spatial curvature of the harmonic phase in the source plane, that tends to considerably increase θ_n/θ_L . This curvature typically results from the dependence of the harmonic phase on the spatially-varying driving laser intensity. This detrimental effect occurred in both experiments described above, where the so-called intrinsic phase of the harmonics is known to depend in both cases on the driving laser intensity. This effect can be compensated at least partially by using spatially-curved wavefronts for the driving laser, which is easily achieved by placing the generation medium slightly out-of-focus (see e.g. [50, 51]). Another possible approach would consist in using a top-hat laser intensity profile at focus, which is in principle possible, but not so simple in practice, in particular with high-power lasers such as those used for HHG from plasmas.

Other solutions are possible, which are more specific to particular generation mechanisms. In the case of HHG in gases, WFR can be implemented in combination with $\omega - 2\omega$ mixing. By reducing the repetition rate of the attosecond pulse emission, this relaxes the condition on the ratio θ_n/θ_L required to get an attosecond lighthouse by a factor of 2 ($p = 1$ instead of 2 in equation (4)). With this combination, attosecond lighthouses could be generated in gases with pulses twice longer than in the previous experiment, i.e. 10 fs or longer. Pulses in the 20 fs range might even be adequate by simultaneously minimizing the ratio θ_n/θ_L , using one of the approaches previously described.

In the case of plasmas, another physical mechanism can lead to the generation of attosecond pulses, which is in certain conditions more favourable than CWE for the attosecond lighthouse scheme. This mechanism is the ROM process, in which the laser-driven periodic oscillation of the plasma mirror surface induces a periodic Doppler effect on the reflected light, leading to a conversion of a part of the laser field energy to higher frequencies [52]. This frequency conversion becomes efficient when the oscillation motion involves relativistic velocities, which typically occurs for laser intensities exceeding $10^{18} \text{ W cm}^{-2}$ at 800 nm. XUV light is generated each time the plasma surface moves outward, which only occurs in a small fraction of the laser optical period. The emission therefore occurs in the form of a train of attosecond pulses.

For this emission mechanism, the spatial phase of the harmonics originates from the denting of the plasma surface,

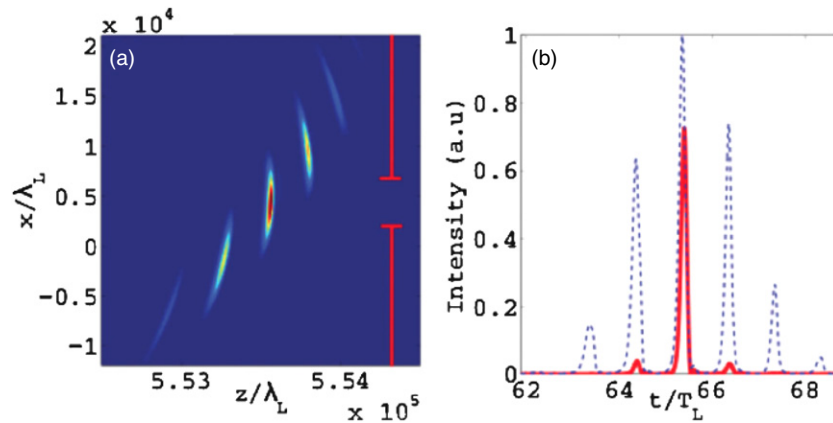


Figure 18. PIC simulation of an attosecond lighthouse generated by the ROM mechanism, where a driving laser pulse of 17 fs initial pulse duration is used at optimal WFR velocity. Panel (a) shows that all the XUV beamlets are well-separated angularly. Therefore a single pulse with a good temporal contrast can be selected with a slit, as presented in (b), where the blue dashed line shows the spatially-integrated intensity temporal profile of the attosecond pulse train in the absence of WFR, and the red line shows the spatially-integrated intensity temporal profile of pulse filtered by the slit in the case with WFR. Reprinted with permission from [16]. Copyright 2011 American Physical Society.

under the effect of the spatially-inhomogeneous radiation pressure and ponderomotive force exerted by the laser as it reflects on the surface [51, 53]. Because the plasma is typically highly-overdense in these experiments, this denting, and hence the spatial phase it induces on the harmonic beam, remain limited if the density gradient at the plasma surface is very steep [51, 54]. When this is not the case, it can be well compensated by slightly defocusing the driving laser beam [51] as long as the laser intensity does not reach the ultrarelativistic regime, i.e. $I \lesssim 10^{20} \text{ W cm}^{-2}$ at 800 nm typically. In these conditions, values of θ_n/θ_L smaller than 0.1 can be achieved, so that attosecond lighthouses should be obtained with laser pulse durations in the 20 fs range. This has been confirmed with 2D PIC simulations where ROM attosecond pulses were generated by a 17 fs driving laser pulse with a PFT optimizing the WFR velocity (figure 18) [16], on a plasma mirror with a very steep interface (density gradient scale length $\lambda_L/200$).

In the longer term, there are more speculative extensions of the attosecond lighthouse scheme. In particular, one exciting question is whether it is possible to use WFR to induce a time-to-angle mapping on the electron beams generated when an intense laser interacts with a target, in order to obtain a collection of ultrashort—potentially attosecond—electron bunches, i.e. a kind of ‘electron machine gun’.

4. Ultrafast measurements using photonic streaking

In the last decade, HHG has been increasingly exploited as a new, highly nonlinear spectroscopic scheme to gather information on the generation medium, in particular to study molecules in the gas phase: an intense laser pulse generates harmonics in a medium, and the properties of the harmonic emission (e.g. spectral intensity and phase, polarization) carry information on the generation medium, e.g. on the molecular orbitals involved in the generation. From this point of view, the collection of attosecond beamlets that can be

produced by applying WFR to the driving laser pulse provides a direct means of adding temporal resolution, within the driving laser pulse, to this spectroscopic scheme, with limited perturbation of the generation process. This approach for ultrafast measurements has been called ‘photonic streaking’ [18]. The underlying principle and its implementation are the same as described in the previous sections, but the collection of attosecond beamlets is now exploited in a totally different way—no longer as a light source, but as a source of additional information.

We first describe the basic idea of this measurement scheme, then summarize the key results of its first experimental demonstration in gases, and finally discuss possible applications and extensions for the future.

4.1. General idea: angular mapping of the temporal dynamics

In conventional optics, fast temporal measurements can be achieved using different types of streak cameras. Among these, mechanical streak cameras use a rotating mirror [55] as shown in figure 19(a). The incoming light pulse is reflected by a rotating mirror, and is deflected into different directions depending on its arrival time on this rotating mirror. The reflected light is thus angularly swept, and the temporal variation of the input light directly mapped on a detector placed at some distance from the mirror, with a typical temporal resolution of a few nano-seconds [55].

Likewise, the key idea of the photonic streaking measurement scheme is to encode temporal information in space, or equivalently in angle, as illustrated in figure 19(b). Rotation velocities considerably higher than those involved in mechanical streak cameras are now obtained by inducing WFR on a femtosecond laser pulse, thus enabling much better temporal resolution, down to the femtosecond range. This pulse then drives HHG in a medium, generating a train of attosecond pulses, each of them carrying information on the generation medium and its interaction with the field at the time of generation. As they propagate in the far-field,

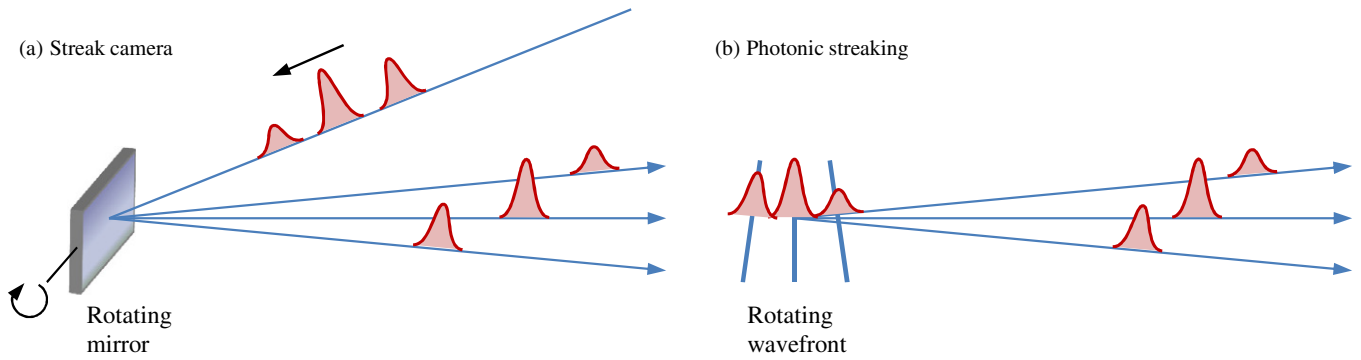


Figure 19. (a) A schematic diagram of a mechanical streak camera that uses a rotating mirror. (b) A schematic diagram of the photonic streaking technique that uses ultrafast wavefront rotation of a femtosecond laser pulse.

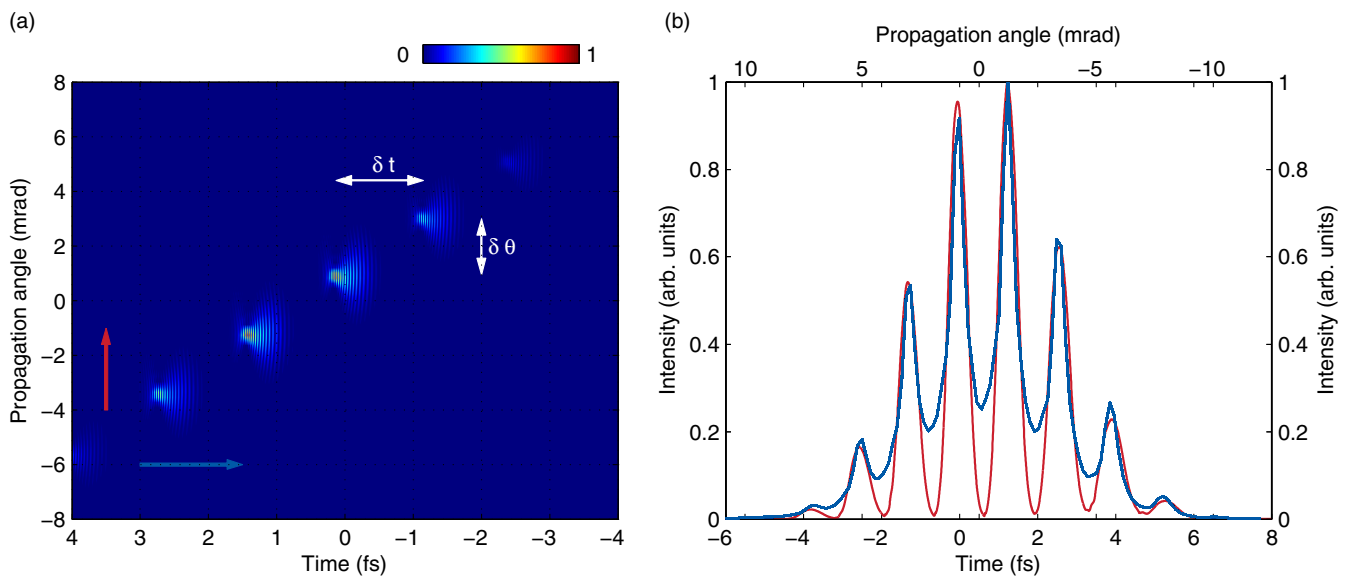


Figure 20. (a) E -field of the attosecond pulse train as a function of space and time in the far-field, in the presence of WFR at focus. The attosecond pulses are calculated from 250 μm -long Ne medium using a Gaussian laser pulse with an intensity of $4.8 \times 10^{14} \text{ W cm}^{-2}$ and 8.5 fs duration at focus. The central wavelength of the laser beam varies from 680 to 850 nm across the beam size of 40 μm (FWHM). Panel (b) shows the temporal intensity profile of the emission (red), obtained by integrating along the propagation angle (i.e. along the red arrow in (a)), and the angular intensity distribution (blue), obtained by integrating along time (i.e. along the blue arrow in (a)). The reduced contrast of the peaks in the blue curve compared to those in the red curve is due to the fact that photonic streaking measures a convolution of the temporal profile of the attosecond pulse train with the angular profile of the attosecond pulses.

these attosecond pulses separate angularly: this enables direct measurements of their individual properties, which thus gives access to time-resolved information along the driving laser pulse. Here, the angular sweeping is optically induced and controlled—hence the name ‘photonic streaking’ [18].

We now illustrate the spatial mapping of a temporal evolution in photonic streaking, with a simulation of HHG in gases, now performed with the simple model described in the first part of the supplementary material of [18]. Figure 20(a) shows a calculated map of the E -field of the generated attosecond pulses as a function of space and time, in the far-field. Successive attosecond pulses are temporally separated by $\delta t = T_L/2$ because HHG in gases repeats every half optical cycle. The number of these pulses and their relative intensity depend on the temporal profile of the driving laser pulse, on the nonlinearity of the generation process, and on the dynamics of the interaction. In a usual HHG experiment, measuring these simple features is possible with established attosecond

temporal measurement techniques, such as FROG CRAB [56], but this remains very demanding experimentally [57].

In contrast, this information is straightforward to obtain using photonic streaking. To demonstrate this idea, an appropriate WFR has been applied on the driving laser pulse in this simulation, to ensure a complete angular separation of the successive pulses. Thus, in figure 20(a) the attosecond pulses are also spatially separated in the far-field. Panel (b) in figure 20 then compares two profiles obtained from this simulation. One is the temporal intensity profile of the attosecond pulse train generated in the medium, and the other the angular intensity profile of the beam, in the presence of WFR. What is remarkable on this graph is the good matching between these two curves, when an adequate scaling of their respective x -axis is used: thus, using WFR, the temporal intensity profile of the emission (number of pulses, relative intensities) is directly obtained by measuring the angular intensity profile of the emission, which is straightforward experimentally.

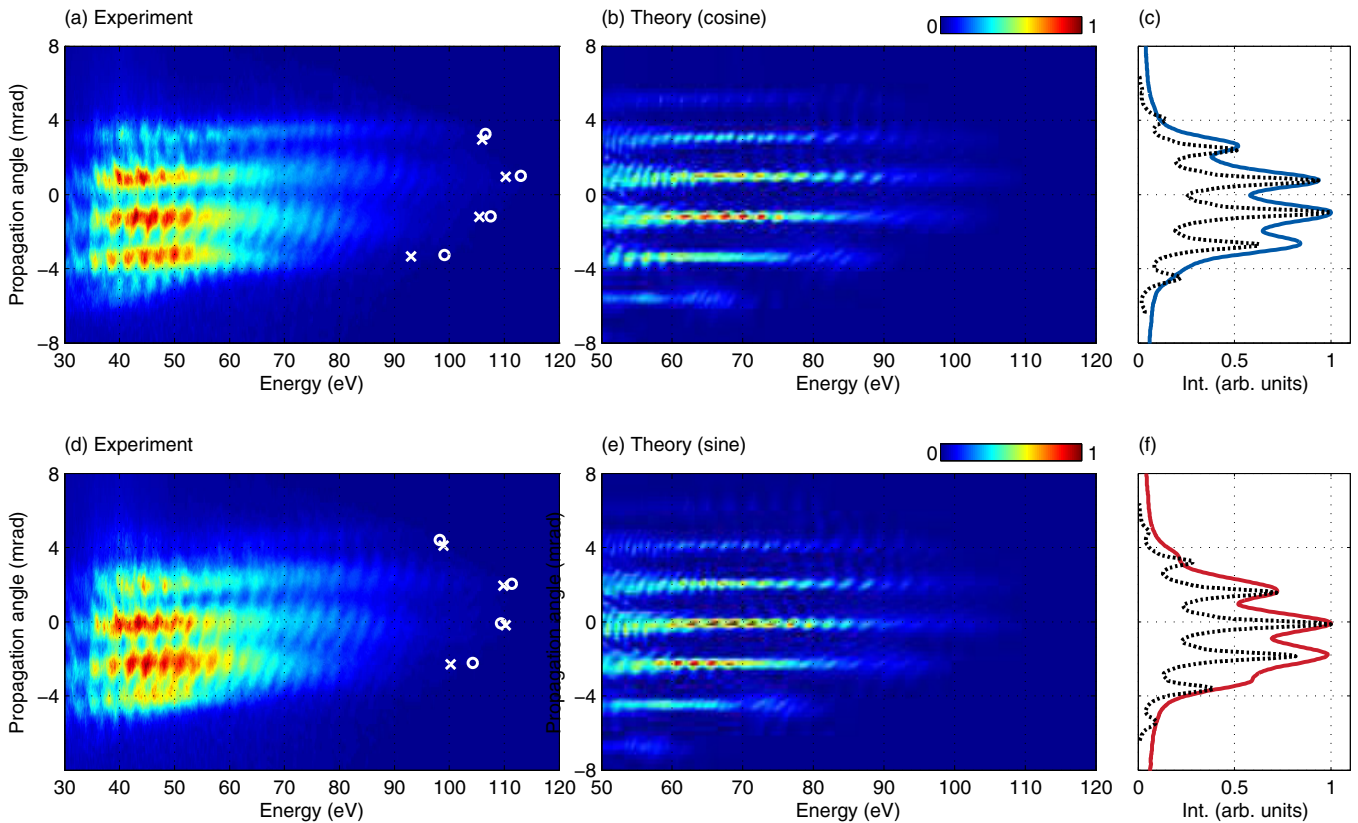


Figure 21. Angularly-resolved spectra of attosecond pulses. (a) The experimental XUV spectrum is obtained from Ne atoms. (b) The XUV spectrum is calculated from $250\ \mu\text{m}$ -long Ne medium using a cosine 8 fs Gaussian laser pulse with an intensity of $4.8 \times 10^{14}\ \text{W cm}^{-2}$ at focus. The central wavelength of the laser beam varies from 680 to 850 nm across the beam size of $40\ \mu\text{m}$ FWHM. (c) The experimental (solid line) and theoretical (dotted line) angular distribution are obtained from (a) and (b). (d) The experimental XUV spectrum is obtained from Ne atoms. The CEP of the laser pulse is changed from (a) by 90° . (e) The XUV spectrum is obtained with the same laser pulse with sine waveform. (f) The experimental (solid line) and theoretical (dotted line) angular distribution obtained from (d) and (e) as explained in [18], the reduced contrast of the modulations in the experimental spatial profiles in (c) and (f) is due to significant residual CEP fluctuations of the driving laser (500 mrad RMS, see section 5.3.). Reprinted with permission from [18]. Copyright 2013 Nature Publishing Group.

Much more information can be obtained by performing more elaborate measurements on the individual beamlets separated by photonic streaking, as will be illustrated in the next subsection. Combining photonic streaking with the different techniques that are now available for XUV and attosecond metrology should make it possible in the near future to measure, for all individual attosecond pulses generated along the laser pulse, properties such as the duration, wavefront or polarization state.

4.2. Experimental evidence

We now summarize the results that have been obtained in the first experiment that has exploited photonic streaking to investigate HHG in gases [18]. This experiment consisted in simultaneously measuring the individual spectra of all attosecond pulses of the train generated in a gas jet. This measurement was possible thanks to the spatial separation of these pulses in the far field induced by photonic streaking. This directly provided spectrograms of the generated attosecond pulse trains, and has confirmed that photonic streaking can be used to measure the relative intensities of the attosecond pulses in the train, as discussed in the previous subsection,

as well as the temporal evolution of spectral features such as the maximum emitted photon energy in each laser half-period (spectral cut-off).

In HHG from gases, the maximum kinetic energy of the recombining electron is determined in first approximation by the instantaneous intensity of the laser pulse at the half cycle where the recombination occurs. For few cycle laser pulses, this instantaneous intensity rapidly changes for every half cycle, and the maximum frequency of the attosecond pulses is thus also expected to rapidly vary, leading to what has been called half-cycle spectral cut-offs [34]. This variation is directly observed in figure 21(a) and (d), which shows the angularly-resolved XUV spectra measured experimentally for each attosecond pulses generated by HHG in a Neon gas jet, by using photonic streaking with a few-cycle driving laser pulse. Since the exact amplitude of the field that drives the recombining electron wave-packet depends on the CEP for a few-cycle laser pulse, the half-cycle cut-offs are also expected to vary with the CEP. This variation is observed from panels (a) to (d) of figure 21, between which a $\pi/2$ change in CEP has been induced on the driving laser pulse.

These measurements can be compared to the predictions of numerical simulations. Figures 21(b) and (e) show the

angularly-resolved HHG spectra calculated with cosine and sine laser pulses, in conditions comparable to those of the experiment. There is a clear qualitative agreement between the simulation results and the experimental ones. For a more quantitative comparison, we define the maximum frequency of each half optical cycle as the frequency where the intensity is 1.5% of the maximum XUV intensity, and mark this frequency in figure 21 with crosses for simulations, and circles for experiment. A good quantitative agreement is observed between the two. The evolution of the half-cycle cut-offs clearly shows the difference in dynamics resulting from cosine or sine driving laser pulses. In figure 21(a), a single maximum half-cycle cut-off is observed, which implies that the cosine laser pulse is used for HHG. As we change the CEP of the laser by $\pi/2$, two maxima are now observed in figure 21(d) which corresponds to the spectrum obtained with a sine laser pulse.

These angularly-resolved HHG spectra can also be used to determine the temporal intensity profile of the attosecond pulse train, simply by integrating the measured signal over a certain spectral bandwidth in the XUV spectrum. The temporal profiles obtained for cosine and sine pulses are shown in panels (c) and (f) of figure 21. Near the peak of the laser pulse where the intensity does not change much, the ionization rate is the most important factor that determines the intensity of the emitted attosecond pulses. As a result, one expects to observe the most intense attosecond pulse(s) to be emitted on the half-cycle(s) that follows the highest spectral cut-off(s). This is precisely what is observed in simulations, but also in the experiment (figures 21(c) and (f)). Note that some discrepancies are nonetheless observed between the theoretical calculation and the experiment. This might be attributed to the assumptions of the theoretical calculation, which considers a perfect Gaussian laser pulse. In contrast, in the experiment the laser pulse may not only be asymmetric in time but, for such few-cycle durations, is also likely to exhibit residual uncontrolled STC at focus (in addition to the applied linear spatial chirp) [58], which were not taken into account in the simulation.

We finally use photonic streaking to study the ionization dynamics of the medium. To this end, measurements were performed in conditions similar to the previous results, but now in N_2 which has a lower ionization potential. Figure 22 is obtained with a single laser shot at three different intensities, 2.4 , 3.4 and $4.5 \times 10^{14} \text{ W cm}^{-2}$. As the laser intensity is increased, the attosecond pulse generation is progressively suppressed in the tail of the pulse, and only occurs in its leading edge. When the emission is spectrally filtered around the spectral cut-off, a single attosecond pulse is obtained as shown figure 22(c). This is a direct observation of ionization gating, which in the present conditions can be attributed to a combination of ground state depletion and phase matching effects.

To conclude this subsection, we note that several features of the emission process observed in this experiment, such as half-cycle cut-offs or ionization gating, had already been reported in several previous experiments, using more complex diagnostics or more sophisticated data analysis. But

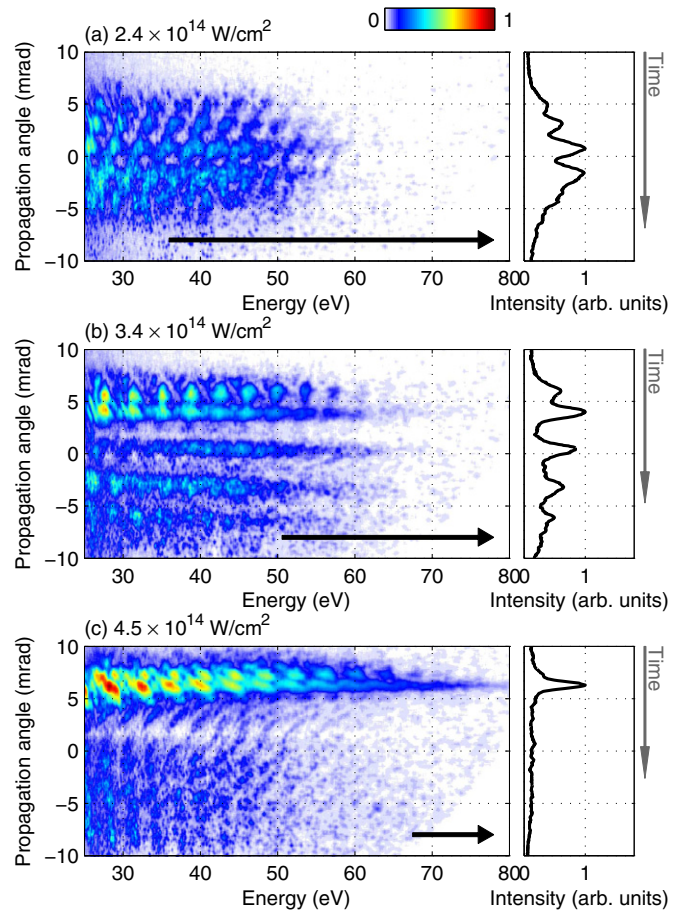


Figure 22. Ionization gating probed by photonic streaking. (a), (c), Angularly resolved XUV spectra measured in N_2 in a single laser shot with a spatial chirp. The peak intensities of the laser pulses are estimated to be 2.4×10^{14} , 3.4×10^{14} and $4.5 \times 10^{14} \text{ W cm}^{-2}$ for (a)–(c), respectively. The curves in the right panels show the normalized angular profile of the XUV beam in each case. These profiles were obtained by integrating the angularly resolved XUV spectra around the cutoff, over the energy ranges indicated by the black arrows, which correspond to energies higher than 60% of the cutoffs expected from the peak intensities of the laser pulse. Reprinted with permission from [18]. Copyright 2013 Nature Publishing Group.

this experiment was really the first to provide such direct measurements of these features, with a technique that is simple to implement and provides results that are straightforward to analyse. As discussed in the next subsection, photonic streaking thus opens up many other possibilities for the future, for instance to measure other properties of the emission, in different generation conditions or for other generation mechanisms.

4.3. Future applications

Many future applications of photonic streaking can be foreseen for HHG in gases. As illustrated by the results of figure 22, its simplicity and single-shot capability make it a very useful tool to study the influence of the generation conditions (e.g. laser intensity, gas density, medium length) on the temporal profile of the emitted attosecond pulse train. This in particular provides a powerful new experimental approach to study the

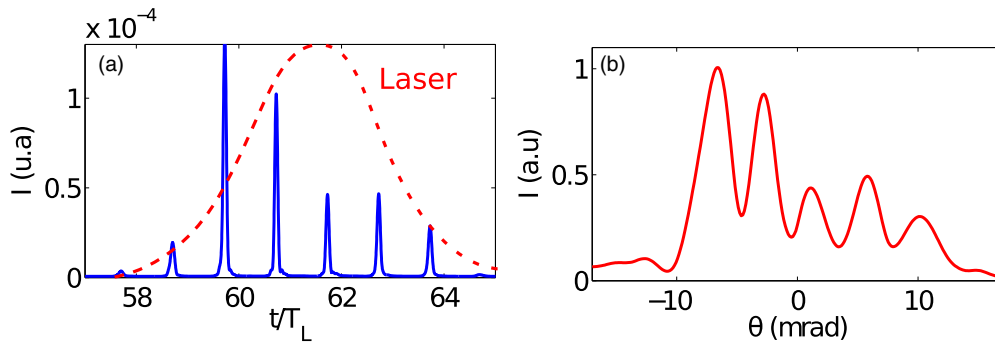


Figure 23. Illustration of the application of photonic streaking to investigate the dynamics of plasma mirrors in the relativistic regime. These curves are obtained from 2D PIC simulations, for a Gaussian laser pulse of initial duration $5T_L$ and peak intensity is $8 \times 10^{19} \text{ W cm}^{-2}$ (at 800 nm), impinging a plasma of density $200n_c$, with a density gradient scale length of $\lambda_L/20$, at 45° in p -polarization, with a waist of $9\lambda_L$. Panel (a) displays the temporal intensity profile of the attosecond pulse train generated through the ROM mechanism. Due to the complex dynamics of the plasma, the most intense attosecond pulses are not emitted at the maximum of the laser pulse. In panel (b), this peculiar temporal profile is mapped onto a spatial profile—much more straightforward to measure experimentally—using photonic streaking.

effect of phase matching on the emission, with time resolution within the driving laser pulse [59].

Photonic streaking will also find important applications in HHG spectroscopy. For instance, in the case of oriented polar molecules, the properties of the harmonic emission is different for successive laser half-cycles, because the recolliding electron wave-packets hit different sides on the asymmetric parent molecules [60, 61]. Using photonic streaking, the corresponding attosecond pulses can be spatially separated and individually characterized, thus providing additional information on the molecules and their asymmetry.

Photonic streaking can also be exploited to investigate other HHG mechanisms, such as those occurring on plasma mirrors [26]. In these experiments, the requirement of target refreshment, and the limited repetition rate and stability of the lasers that are typically used, make it difficult to implement the most advanced measurement techniques of XUV and attosecond metrology, especially when a large number of shots are needed, for instance to scan a parameter. As a result, very little information has for instance been obtained experimentally so far on the temporal dynamics of HHG from plasma mirrors. Photonic streaking will be particularly useful for such experiments. We illustrate this potential by considering the results of PIC simulations displayed in figure 23.

In this simulation, the attosecond pulses are generated by the ROM mechanism, each time a relativistic electron jet is emitted towards vacuum (figure 23(a)). In the regime of this simulation, the B -field of the laser plays a crucial role, and actually inhibits the emission in the most intense part of the laser pulse, due to the gyromagnetic effect described in [62]. In addition, ion motion during the laser pulse affects the plasma density profile, in such a way that the attosecond pulse emission is strongly reduced in the trailing edge of the pulse. The combination of these effects results in a highly non-trivial intensity profile of the attosecond pulse train, displayed in figure 23(a), where the most intense attosecond pulse is actually emitted in the very leading edge of the laser pulse. While it would be extremely difficult to measure with other techniques, this effect can be easily diagnosed with photonic streaking, as illustrated in figure 23(b): when WFR is used

to angularly separate the attosecond pulses of the train, the angular intensity profile of the emission maps very well the temporal intensity profile of the emission, just like for HHG in gases (figure 20). Another potential use of photonic streaking for the study of plasma mirrors will be to time-resolve the attosecond pulses emitted in each laser cycle by the ROM and CWE mechanisms, and study the evolutions of their spectrum, emission times and relative intensity, with parameters such as the plasma density gradient scale length or laser intensity, thus providing a detailed picture of the laser-plasma interaction dynamics in actual experiments.

We conclude this section by discussing qualitatively two interesting points, which will require further studies. First of all, it is interesting to wonder whether or not the photonic streaking scheme can also provide information on the duration, or even the temporal structure, of the individual attosecond pulses in the train. This question has not been studied in detail yet, but qualitatively one can expect the WFR to be too slow to provide temporal resolution on the attosecond scale. And indeed, we emphasized in subsection 3.2 that the individual attosecond pulses are not affected by WFR, which would be a pre-requisite to get information on their temporal structure. Reaching attosecond resolution with photonic streaking will require finding schemes to achieve faster WFR in the medium, for instance through $\omega - 2\omega$ mixing [28].

The second point is that photonic streaking can still provide temporal information even when the angular separation of successive attosecond pulses in the train is not complete. Such an incomplete separation will typically occur when ‘long’ driving laser pulses are used for the generation, such that the criterion of equation (4) is not fulfilled. Even in this case, WFR still induces a mapping of time on propagation angle, implying that different temporal sections of the attosecond pulse train are sent in slightly different directions (see results of PIC simulation in figure 24, panel (a)). If for instance the attosecond pulses in the train are unevenly spaced (‘femtosecond chirp’), this will result in tilted harmonics in the angularly-resolved harmonic spectrum, as observed in the simulation of figure 24 (panel (b)), and this tilt provides information on the harmonic chirp. Such a tilt has already been observed in experiments (figure 25) for

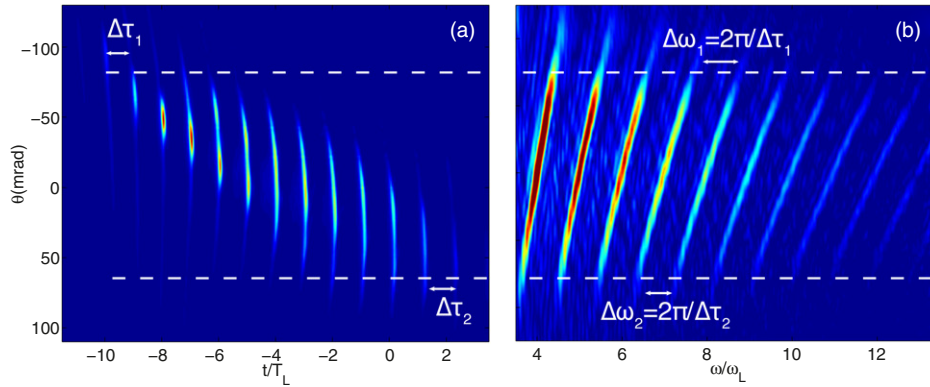


Figure 24. 2D PIC simulation of photonic streaking in the CWE regime with a ‘long’ (15 fs) driving laser pulse. Panel (a) shows the intensity distribution of the attosecond pulses after diffraction from the source, as a function of time and propagation angle. The time-to-angle mapping induced by photonic streaking is clearly observed across the pulse train, but is not sufficient to fully separate the successive attosecond pulses angularly. CWE generates a pulse train with a femtosecond chirp, which originates from the uneven spacing of the attosecond pulses along the train [50]. This spacing varies from ΔT_1 to ΔT_2 between the two ends of the train. Panel (b) shows the angularly-resolved harmonic spectrum obtained in this simulation. The combination of the femtosecond chirp of the train and of the time-to-angle mapping induced by photonic streaking results in tilted harmonics. Each tilted ellipse can be considered as a spectrogram of the harmonic field.

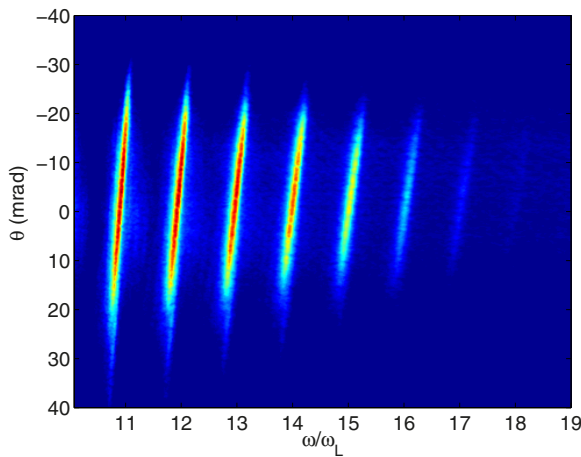


Figure 25. Angularly-resolved CWE harmonic spectrum measured with the UHI100 laser of CEA-IRAMIS (100 TW-25 fs), when PFT is applied to the pulse before focusing. A tilt of the harmonics is observed, as in the simulation of figure 24 (panel (b)), which might be used to retrieve the femtosecond chirp of each individual harmonic.

CWE harmonics from plasma mirrors. Further studies are now needed to determine the exact temporal information that can be extracted in this measurement regime.

5. Carrier–envelope relative phase metrology

In this last section, we briefly discuss the effect of the driving laser CEP on HHG in the presence of WFR, and its potential applications for CEP metrology [33, 34, 63–65].

5.1. Key idea

The main effect of a change in the CEP of a laser pulse driving HHG in any medium is a shift in time of the generated attosecond pulse train, since the attosecond pulses are generated around certain phases of the laser field. As

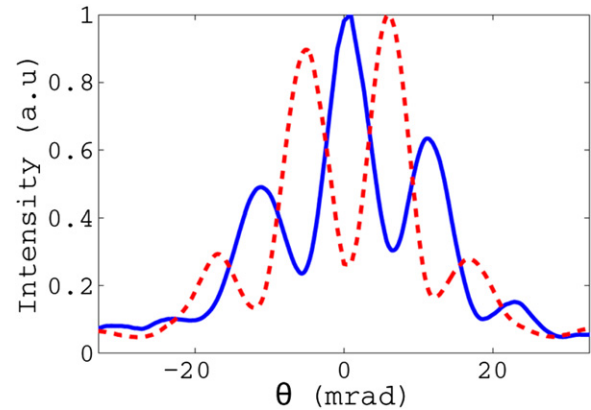


Figure 26. Sensitivity of the spatial distribution of the attosecond beamlets to the CEP of the driving laser, in the case of plasma mirrors. The curves display the spatial profile of the spectrally-integrated harmonic signal (from orders 25 to 30) in the far field, for two values of the driving-laser pulse CEP differing by π , obtained from PIC simulations, for the same physical parameters as in figure 18 (generation in the ROM regime). Reprinted with permission from [16]. Copyright 2011 American Physical Society.

discussed in the previous section, in the presence of WFR, emission time is mapped onto propagation angle. Therefore, in this case, any change in CEP should result in a shift in propagation angle of all the attosecond beamlets [16]. This effect has been observed very clearly in simulations, both for HHG in gases and from plasmas, as shown in figures 26 and 27. We now turn to the experimental evidence of this effect, also obtained both for HHG in gases and from plasmas.

5.2. Experimental evidence

Figures 28 and 29 respectively show the effect of a change in the laser CEP in the experiments performed on plasma mirrors and in gases. In both cases, the CEP was varied by slightly translating one wedge of the pair shown in figures 10 and 12 with respect to the other. In the first case, the data

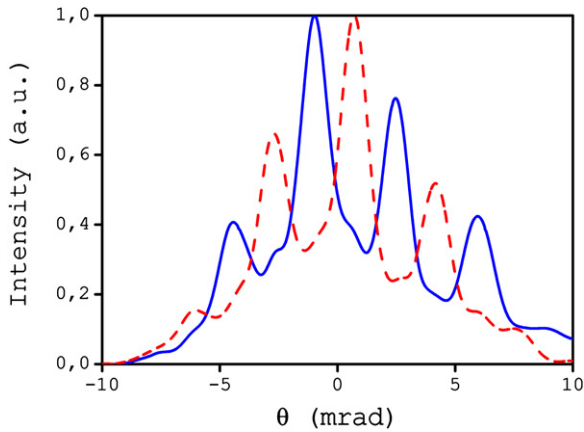


Figure 27. Sensitivity of the spatial distribution of the attosecond beamlets to the CEP of the driving laser, in the case of HHG in gases. The curves display the spatial profile of the spectrally-integrated harmonic signal (from orders 20–120) in the far field, for two values of the driving-laser pulse CEP now differing by $\pi/2$, obtained from numerical simulations using the code described in section II of the supplementary information of [18], for the same physical parameters as in figure 16, but at a slightly higher intensity ($8.5 \times 10^{14} \text{ W cm}^{-2}$).

show the 2D spatial profile of the emitted beamlets, frequency-filtered around a group of harmonics, for different changes in CEP [17]. The angle of propagation of all attosecond pulses clearly drift linearly as the CEP is scanned. The last image in figure 28 illustrates how, due to this sensitivity to CEP, the spatial pattern gets blurred when multiple laser-shots are accumulated without CEP stabilization.

A similar effect of CEP is observed in the case of gases [18], in figure 29, which now shows lineouts of the angular intensity profile of the emission, frequency-integrated over the whole energy range, along the direction of WFR, as a function of the CEP variation. These experimental observations are fully consistent with numerical simulations, and clearly demonstrate the influence of the CEP in the presence of WFR.

This experimental observation is conceptually important, because it provides a direct demonstration of the time-to-space mapping induced by WFR, and also provides a calibration of

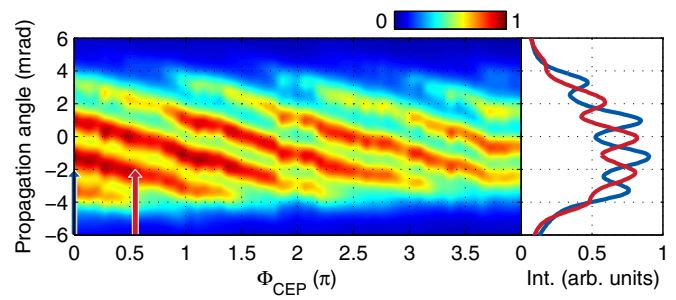


Figure 29. Experimental observation of the effect of CEP in gases. The colour code shows the spatial profile of the XUV beam (averaged over 30 laser shots), in the presence of wavefront rotation, as a function of the CEP of the driving laser pulse. Right panel: two lineouts at two particular CEPs differing by $\pi/2$, which shows the same effect as in the simulations of figure 27. Reprinted with permission from [18]. Copyright 2013 Nature Publishing Group.

this mapping. Figure 28 for instance proves that the angular separation between two adjacent beamlets, which is swept by a 2π phase shift of the laser field, corresponds to one laser period $T_L = 2.6 \text{ fs}$. Therefore, the individual well-separated beamlets necessarily have a duration shorter than this optical period. This constitutes the most direct evidence so far that attosecond pulses are indeed associated to HHG from plasmas. As discussed in the previous section, the duration of these attosecond pulses can however not be deduced from these data.

We now discuss in the next subsection why this effect of CEP is also important from a technical point of view.

5.3. Future applications

The first practical consequence of this effect of CEP is that lasers with CEP stabilization are required to generate *stable* attosecond lighthouses from any medium. But on the other hand, this effect can also be exploited to track CEP changes right in the generation medium, for every single laser shot. This idea is illustrated by the experimental results of figure 30, obtained in a gas jet.

The left panel of this figure shows a collection of successive angular intensity profiles of the attosecond beamlets

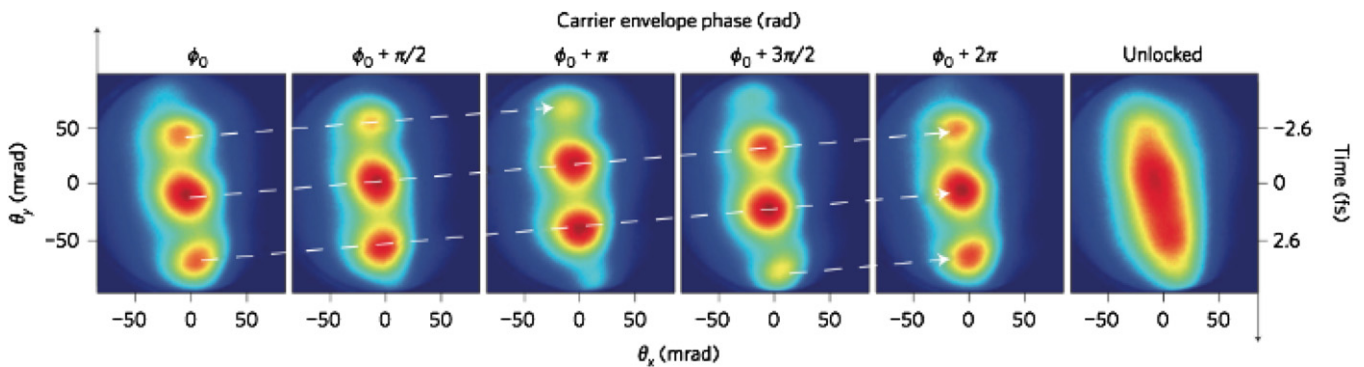


Figure 28. Experimental observation of the effect of CEP for plasma mirrors. These spatial patterns show the progressive change in direction of emission of the isolated attosecond beamlets produced by the attosecond lighthouse effect, for increasing values of the relative CEP of the laser. The rightmost image shows blurring of the EUV spatial beam profile arising from the generation of attosecond pulses in uncontrolled directions as the waveform of the laser randomly fluctuates from shot-to-shot when the laser CEP is not locked. All images are an accumulation of 300 consecutive shots. Reprinted with permission from [17]. Copyright 2012 Nature Publishing Group.

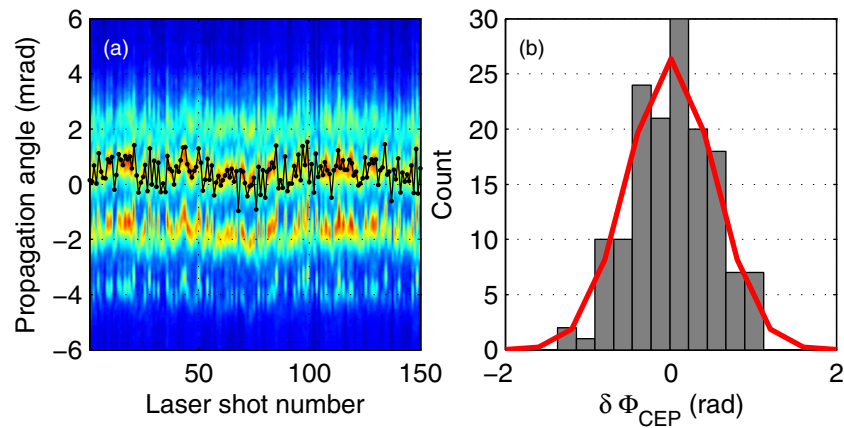


Figure 30. The colour map (a) shows 150 successive single-shot spatial profiles of the XUV beamlets. The black line with dots shows the shot-to-shot fluctuations of the central position of one of the beamlets, and reveals the residual CEP jitter in the generation medium. This effect provides a direct way of determining the CEP statistics in this medium, displayed in panel (b), leading to a standard deviation of the CEP of ≈ 500 mrad in our experiment. Reprinted with permission from [18]. Copyright 2013 Nature Publishing Group.

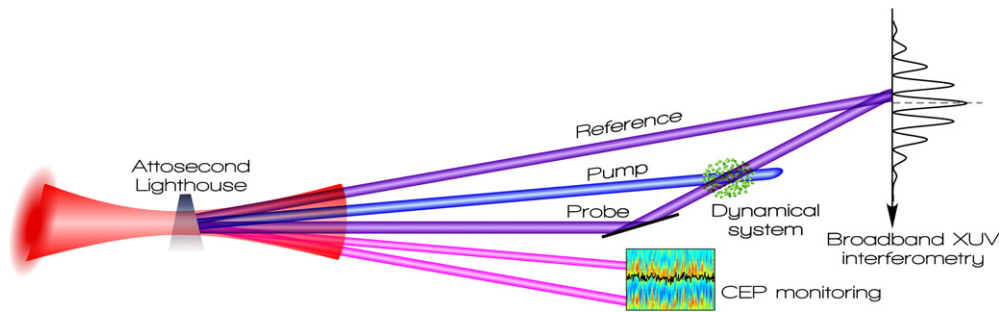


Figure 31. Sketch of principle of an experiment exploiting different features of an attosecond lighthouse source, for advanced pump-probe experiments where both amplitude and phase perturbations induced on the probe are measured.

generated with WFR, each obtained in a single laser shot. The angular positions of these beamlets fluctuate from shot-to-shot. During these measurements, the stabilization loop for the laser CEP was turned on: these changes are thus due to residual fluctuations in CEP, in the generation medium. Using these positions as a diagnostic, the statistics of these residual CEP fluctuations can be reconstructed, as shown in figure 30(b). While several techniques are now well-established to track CEP changes [63–65], this is to the best of our knowledge the first time that these changes are measured directly at the point of interaction of the laser with the target.

This scheme opens promising perspectives from a technical point of view. In future experiments, single-shot measurements of the beamlets positions could for instance be used as a feedback signal to actively stabilize the CEP of the laser pulse right in the generation medium, and achieve unprecedented CEP stabilities in this medium. Alternatively, in cases where the CEP is not or only poorly stabilized, these positions could also be used to tag the CEP for each laser shot. This would be particularly useful for high-power lasers such as those used for HHG from plasmas, for which CEP stabilization is extremely difficult, if not impossible when they have a low-repetition rate. Such tagging of the CEP would make it possible to study CEP-dependent phenomena without CEP stabilization, and would release the constraint on CEP stability to use attosecond lighthouses as light sources.

To conclude this part, we would like to emphasize that we have always referred here to CEP changes, and not to absolute

values of the CEP. This is because, in the presence of WFR, such an absolute value of the CEP can no longer be defined for the driving laser pulse. This is best understood by considering the laser pulse before focusing: since the pulse front is tilted with respect to the wavefront, the local value of the CEP varies across the beam, potentially by several times 2π . At focus, the indeterminacy of the CEP comes from the spatial chirp, which implies that the frequency of the carrier wave varies across the focal spot, while the pulse envelop remains unchanged. Strictly speaking, it is thus impossible to define a single value of the CEP for a pulse with PFT or spatial chirp. But changes in CEP, which affect the laser phase by the same value everywhere in time and space, remain perfectly meaningful.

6. Conclusion

We have described the basics of ultrafast wavefront rotation (WFR) of femtosecond laser pulses, and discussed different schemes in which this spatio-temporal coupling can be exploited in highly nonlinear optics, all of which have recently been demonstrated experimentally. We have extensively discussed several future applications of these schemes, which largely remain within reach of the present state-of-the-art of high-field science and ultrafast science. Looking further ahead, more ambitious—but also more challenging—experiments exploiting WFR in highly nonlinear optics can be envisioned, which combine several of the ideas discussed in this paper. In

particular, an advanced scheme for future attosecond pump-probe experiments is proposed in figure 31.

This scheme uses an attosecond lighthouse that generates at least five well-separated attosecond beamlets. Like in figure 17, one of these beamlets is used as a pump beam to trigger an ultrafast dynamics in a medium, and a second beamlet is used as a probe to time-resolve this dynamics. A third beamlet of the lighthouse is then used as a reference beam, to measure both the amplitude and the phase perturbations induced on the probe by this dynamics, using for instance time- and frequency-resolved broadband XUV interferometry between the probe and the reference. Two beamlets or more are finally used either to track CEP changes in the generation medium, or to stabilize this CEP with high-accuracy right in this medium to optimize the reproducibility of the attosecond source. Such an experiment is of course challenging, but considering the considerable progresses achieved by attosecond science in the past decade, it could be within reach in the coming decade.

As a general conclusion, this work points to an important new direction in high-field and ultrafast sciences. While spatio-temporal couplings of ultrafast laser beams have so far mostly been considered as detrimental, the use of WFR in highly nonlinear optics illustrates how shaping light fields in both time and space can provide new degrees of freedom for laser-matter interaction experiments, leading to new experimental capabilities. And indeed, other applications of spatio-temporal couplings have recently been identified, such as spatio-temporal focusing of ultrashort laser pulses, where a spatial chirp is initially applied to the unfocused beam, leading to pulse front tilt at focus—just the reverse of the configuration considered in this paper. The intensity distribution along the z -axis of such a beam is much more peaked than for a conventional STC-free beam, allowing for a more localized nonlinear interaction with extended media. This has already found applications in nonlinear microscopy [66, 67], micromachining [68, 69] and waveguide writing. These recent developments suggest that the metrology and control of STC should become a major challenge of ultrafast optics for the coming years, and that exploring the use of STC should open many new avenues in different fields of laser-matter interaction science where broadband laser pulses are used.

References

- [1] Corkum P B and Krausz F 2007 Attosecond science *Nature Phys.* **3** 381–7
- [2] Krausz F and Ivanov M Y 2009 Attosecond physics *Rev. Mod. Phys.* **81** 163
- [3] Mourou G, Tajima T and Bulanov S 2006 *Rev. Mod. Phys.* **78** 309–71
- [4] Antoine P, L’Huillier A and Lewenstein M 1996 Attosecond pulse trains using high-order harmonics *Phys. Rev. Lett.* **77** 1234–7
- [5] Paul P, Toma E, Breger P, Mullot G, Augé F, Balcou P, Muller H and Agostini P 2001 Observation of a train of attosecond pulses from high harmonic generation *Science* **292** 1689–92
- [6] Kienberger R *et al* 2003 Atomic transient recorder *Nature* **427** 817–21
- [7] Sansone G *et al* 2006 Isolated single-cycle attosecond pulses *Science* **314** 443
- [8] Mashiko H, Gilbertson S, Li C, Khan S D, Shakya M M, Moon E and Chang Z 2008 Double optical gating of high-order harmonic generation with carrier-envelope phase stabilized lasers *Phys. Rev. Lett.* **100** 103906
- [9] Goulielmakis E *et al* 2008 Single-cycle nonlinear optics *Science* **320** 1614–7
- [10] Feng X, Gilbertson S, Mashiko H, Wang H, Khan S D, Chini M, Wu Y, Zhao K and Chang Z 2009 Generation of isolated attosecond pulses with 20 to 28 femtosecond lasers *Phys. Rev. Lett.* **103** 183901
- [11] Sansone G, Poletto L and Nisoli M 2011 High-energy attosecond light sources *Nature Photon.* **5** 655–63
- [12] Akturk S, Gu X, Bowlan P and Trebino R 2010 Spatio-temporal couplings in ultrashort laser pulses *J. Opt.* **12** 093001
- [13] Akturk S, Gu X, Gabolde P and Trebino R 2005 The general theory of first-order spatio-temporal distortions of Gaussian pulses and beams *Opt. Express* **13** 8642–61
- [14] Thaury C and Quéré F 2010 *J. Phys. B: At. Mol. Opt. Phys.* **43** 213001
- [15] Bourassin-Bouchet C, Stephens M, de Rossi S, Delmotte F and Chavel P 2011 Duration of ultrashort pulses in the presence of spatio-temporal coupling *Opt. Express* **19** 17357–71
- [16] Vincenti H and Quéré F 2012 Attosecond lighthouses: how to use spatiotemporally coupled light fields to generate isolated attosecond pulses *Phys. Rev. Lett.* **108** 113904
- [17] Wheeler J A, Borot A, Monchocé S, Vincenti H, Ricci A, Malvache A, Lopez-Martens R and Quéré F 2012 Attosecond lighthouses from plasma mirrors *Nature Photon.* **6** 829–33
- [18] Kim K T, Zhang C, Ruchon T, Hergott J-F, Auguste T, Villeneuve D, Corkum P and Quéré F 2013 Photonic streaking of attosecond pulse trains *Nature Photon.* **7** 651–6
- [19] Hebling J 1996 Derivation of the pulse front tilt caused by angular dispersion *Opt. Quantum Electron.* **28** 1759–63
- [20] Akturk S, Gu X, Gabolde P and Trebino R 2005 The general theory of first-order spatio-temporal distortions of Gaussian pulses and beams *Opt. Express* **13** 8642–61
- [21] Akturk S, Gu X, Zeek E and Trebino R 2004 Pulse-front tilt caused by spatial and temporal chirp *Opt. Express* **12** 4399–410
- [22] Heyl C *et al* 2013 *Oral Communication, ATTO Conf. (Paris)*
- [23] Heyl C *et al* 2014 Noncollinear optical gating *New J. Phys.* **16** 052001
- [24] Lichters R, Vehn J Meyer-ter and Pukhov A 1996 Short-pulse laser harmonics from oscillating plasma surfaces driven at relativistic intensity *Phys. Plasmas* **3** 3425
- [25] Plaja L, Roso L, Rzazewski K and Lewenstein M 1998 Generation of attosecond pulse trains during the reflection of a very intense laser on a solid surface *J. Opt. Soc. Am. B* **15** 1904–11
- [26] Quéré F, Thaury C, Monot P, Dobosz S, Martin P, Geindre J-P and Audebert P 2006 Coherent wake emission of high-order harmonics from overdense plasmas *Phys. Rev. Lett.* **96** 125004
- [27] Borot A *et al* 2012 Attosecond control of collective electron motion in plasmas *Nature Phys.* **8** 416–21
- [28] Kim K, Zhang C, Shiner A, Kirkwood S, Frumker E, Gariepy G, Naumov A, Villeneuve D and Corkum P 2013 Manipulation of quantum paths for spacetime characterization of attosecond pulses *Nature Phys.* **9** 159–63
- [29] Priori E *et al* 2000 Nonadiabatic three-dimensional model of high-order harmonic generation in the few-optical-cycle regime *Phys. Rev. A* **61** 063801

- [30] Gaarde M B, Schafer K J, Heinrich A, Biegert J and Keller U 2005 Large enhancement of macroscopic yield in attosecond pulse train-assisted harmonic generation *Phys. Rev. A* **72** 013411
- [31] Altucci C, Tisch J and Velotta R 2011 Single attosecond light pulses from multi-cycle laser sources *J. Mod. Opt.* **58** 1585–610
- [32] Chini M, Zhao K and Chang Z 2014 The generation, characterization and applications of broadband isolated attosecond pulses *Nature Photon.* **8** 178–86
- [33] Baltuska A *et al* 2003 Attosecond control of electronic processes by intense light fields *Nature* **421** 611–5
- [34] Haworth C, Chipperfield L, Robinson J, Knight P, Marangos J and Tisch J 2006 Half-cycle cutoffs in harmonic spectra and robust carrier-envelope phase retrieval *Nature Phys.* **3** 52–57
- [35] Corkum P B, Burnett N H and Ivanov M Y 1994 Subfemtosecond pulses *Opt. Lett.* **19** 1870
- [36] Sola I, Mével E, Elouga L and Constant E 2006 Controlling attosecond electron dynamics by phase-stabilized polarization gating *Nature Phys.* **2** 319–22
- [37] Christov I P, Murnane M M and Kapteyn H C 1997 High-harmonic generation of attosecond pulses in the ‘single-cycle’ regime *Phys. Rev. Lett.* **78** 1251–4
- [38] Calegari F, Lucchini M, Negro M, Vozzi C, Poletto L, Svelto O, De Silvestri S, Sansone G, Stagira S and Nisoli M 2012 Temporal gating methods for the generation of isolated attosecond pulses *J. Phys. B: At. Mol. Opt. Phys.* **45** 074002
- [39] Kim K T, Kim C M, Baik M G, Umesh G and Nam C H 2004 Single sub-50-attosecond pulse generation from chirp-compensated harmonic radiation using material dispersion *Phys. Rev. A* **69** 051805
- [40] Abel M, Pfeifer T, Nagel P, Boutou W, Bell M, Steiner C, Neumark D and Leone S 2009 Isolated attosecond pulses from ionization gating of high-harmonic emission *Chem. Phys.* **366** 9–14
- [41] Ferrari F, Calegari F, Lucchini M, Vozzi C, Stagira S, Sansone G and Nisoli M 2010 High-energy isolated attosecond pulses generated by above-saturation few-cycle fields *Nature Photon.* **4** 875–9
- [42] Altucci C, Esposito R, Tosa V and Velotta R 2008 Single isolated attosecond pulse from multicycle lasers *Opt. Lett.* **33** 2943–5
- [43] Altucci C *et al* 2010 Interplay between group-delay-dispersion-induced polarization gating and ionization to generate isolated attosecond pulses from multicycle lasers *Opt. Lett.* **35** 2798–800
- [44] Pfeifer T, Gallmann L and Abel M 2006 Single attosecond pulse generation in the multicycle-driver regime by adding a weak second-harmonic field *Opt. Lett.* **31** 975–7
- [45] Mashiko H, Gilbertson S, Li C and Khan S 2008 Double optical gating of high-order harmonic generation with carrier-envelope phase stabilized lasers *Phys. Rev. Lett.* **100** 103906
- [46] Tsakiris G D, Eidmann K, Meyer-ter-Vehn J and Krausz F 2006 Route to intense single attosecond pulses *New J. Phys.* **8** 19
- [47] Baeva T, Gordienko S and Pukhov A 2006 Relativistic plasma control for single attosecond x-ray burst generation *Phys. Rev. E* **74** 065401
- [48] Naumova N, Nees J, Sokolov I, Hou B and Mourou G 2004 Relativistic generation of isolated attosecond pulses in a $\lambda(3)$ focal volume *Phys. Rev. Lett.* **92** 063902
- [49] Heissler P *et al* 2012 Few-cycle driven relativistically oscillating plasma mirrors: a source of intense isolated attosecond pulses *Phys. Rev. Lett.* **108** 235003
- [50] Quéré F, Thauray C, Geindre J, Bonnaud G, Monot P and Martin P 2008 Phase properties of laser high-order harmonics generated on plasma mirrors *Phys. Rev. Lett.* **100** 095004
- [51] Vincenti H, Monchoce S, Kahaly S, Bonnaud G, Martin P and Quéré F 2014 Optical properties of relativistic plasma mirrors *Nature Commun.* **5** 3403
- [52] Lichters R, Meyer-ter-Vehn J and Pukhov A 1996 Short-pulse laser harmonics from oscillating plasma surfaces driven at relativistic intensity *Phys. Plasmas* **3** 3425–37
- [53] Dromey B *et al* 2009 Diffraction-limited performance and focusing of high harmonics from relativistic plasmas *Nature Phys.* **5** 146–52
- [54] Kahaly S, Monchoce S, Vincenti H, Dzelzainis T, Dromey B, Zepf M, Martin P and Quéré F 2013 Direct observation of density-gradient effects in harmonic generation from plasma mirrors *Phys. Rev. Lett.* **110** 175001
- [55] Landre J 1964 Time resolution of streak cameras equipped with rotating mirrors of beryllium *Rev. Sci. Instrum.* **35** 796–801
- [56] Mairesse Y and Quéré F 2005 Frequency-resolved optical gating for complete reconstruction of attosecond bursts *Phys. Rev. A* **71** 011401
- [57] Kim K T, Ko D H, Park J J, Tosa V and Nam C H 2010 Complete temporal reconstruction of attosecond high-harmonic pulse trains *New J. Phys.* **12** 083019
- [58] Karimi E, Altucci C, Tosa V, Velotta R and Marrucci L 2013 Influence of generalized focusing of few-cycle Gaussian pulses in attosecond pulse generation *Opt. Express* **21** 24991–9
- [59] Rundquist A, Durfee C G, Chang Z, Herne C, Backus S, Murnane M M and Kapteyn H C 1998 Phase-matched generation of coherent soft x-rays *Science* **280** 1412–5
- [60] Kraus P, Rupenyan A and Wörner H 2012 High-harmonic spectroscopy of oriented ocs molecules: emission of even and odd harmonics *Phys. Rev. Lett.* **109** 233903
- [61] Frumker E, Hebeisen C T, Kajumba N, Bertrand J B, Wörner H J, Spanner M, Villeneuve D M, Naumov A and Corkum P B 2012 Oriented rotational wave-packet dynamics studies via high harmonic generation *Phys. Rev. Lett.* **109** 113901
- [62] Geindre J P, Audebert P and Marjoribanks R S 2006 Relativistic AC gyromagnetic effects in ultraintense laser-matter interaction *Phys. Rev. Lett.* **97** 085001
- [63] Jones D J, Diddams S A, Ranka J K, Stentz A, Windeler R S, Hall J L and Cundiff S T 2000 Carrier-envelope phase control of femtosecond mode-locked lasers and direct optical frequency synthesis *Science* **288** 635–9
- [64] Kakehata M, Takada H, Kobayashi Y, Torizuka K, Fujihira Y, Homma T and Takahashi H 2001 Single-shot measurement of carrier-envelope phase changes by spectral interferometry *Opt. Lett.* **26** 1436–8
- [65] Paulus G, Lindner F, Walther H, Baltuška A, Goulielmakis E, Lezius M and Krausz F 2003 Measurement of the phase of few-cycle laser pulses *Phys. Rev. Lett.* **91** 253004
- [66] Oron D, Tal E and Silberberg Y 2005 Scanningless depth-resolved microscopy *Opt. Express* **13** 1468–76
- [67] Zhu G, van Howe J, Durst M, Zipfel W and Xu C 2005 Simultaneous spatial and temporal focusing of femtosecond pulses *Opt. Express* **13** 2153–59
- [68] Vitek D N, Adams D E, Johnson A, Tsai P S, Backus S, Durfee C G, Kleinfeld D and Squier J A 2010 Temporally focused femtosecond laser pulses for low numerical aperture micromachining through optically transparent materials *Opt. Express* **18** 18086–94
- [69] Vitek D N, Block E, Bellouard Y, Adams D E, Backus S, Kleinfeld D, Durfee C G and Squier J A 2010 Spatio-temporally focused femtosecond laser pulses for nonreciprocal writing in optically transparent materials *Opt. Express* **18** 24673–8